TÉCNICO LISBOA

Evaluation of the potential of a gamma-ray observatory to detect astrophysical neutrinos

Pedro Valdez Machado de Jesus Costa

Thesis to obtain the Master of Science Degree in

Engineering Physics

Supervisors: Prof. Ruben Maurício da Silva Conceição
Prof. Jaime Alvarez-Muñiz

Examination Committee

Chairperson: Prof. Dr. Mário João Martins Pimenta
Supervisor: Prof. Jaime Alvarez-Muñiz
Members of the Committee: Prof. Bernardo António Neto Gomes Baptista Tomé
Dr. Sofia Andringa Dias

October 2021

Acknowledgements

I would like to thank everyone that, in one way or another, contributed to the elaboration of the work presented in my thesis.

To Ruben Conceição and Jaime Alvarez-Muñiz, my supervisors, for all the support and assistance even in these unusual times, and for believing in me. A special thanks to Ruben, for supporting me and pushing me to go further since even before the start of this thesis work.

To all my friends, who helped me keep my spirits up, even through the worst of times.

A special thanks to my family: my parents and my sister, who always cheered me up and motivated me to keep moving forward.

Resumo

A descoberta de neutrinos astrofísicos de muito alta energia abriu uma nova janela para o Universo. No entanto, as fontes desses neutrinos ainda são amplamente desconhecidas. Uma abordagem com múltiplos mensageiros é favorecida na busca por essas fontes e para ajudar a responder a perguntas cruciais em astrofísica. Para ajudar neste processo, é importante que os observatórios existentes expandam os limites de suas capacidades de detecção para abranger mais mensageiros.

O objetivo desta tese é determinar se um observatório de raios gama localizado na superfície da Terra é capaz de medir neutrinos com energias entre 100 TeV e 1 PeV, e o desempenho esperado. Os principais objetos de estudo são chuveiros de partículas muito inclinados induzidos por neutrinos de electrões descendentes e ascendentes. O fundo é predominantemente composto de chuveiros muito inclinados induzidos por raios cósmicos. A discriminação entre sinal e fundo é baseada no balanço entre o sinal eletromagnético total e o sinal muónico total no solo.

Demonstramos que um observatório de raios gama de campo amplo com uma escala de km^2 é previsto ser capaz de detectar neutrinos de muito alta energia (tanto neutrinos atmosféricos como astrofísicos) a uma taxa média de 2.09×10^{-1} ano^{-1}, ou ~ 1 evento a cada 5 anos. A maior taxa de evento estimada é 3.72×10^{-1} ano^{-1} ou ~ 1 evento a cada $2-3$ anos.

Palavras-Chave: Neutrinos astrofísicos; Neutrinos atmosféricos; Raios gama; Raios cósmicos; Observatórios de raios gama no solo

Abstract

The discovery of very-high-energy astrophysical neutrinos opened a new window to the Universe. However, the sources of these neutrinos are still largely unknown. A multimessenger approach is favoured in the search for these sources and to help answer long-standing questions in astrophysics. To aid in this process, it is important for existing observatories to expand the limits of their detection capabilities to cover more messengers.

The aim of this thesis is to determine whether a ground-based gamma-ray observatory is capable of measuring neutrinos with energies ranging from 100 TeV to 1 PeV, and its expected performance. The main objects of study are very inclined extensive air showers induced by down-going and up-going electron neutrinos. Background is predominantly made up of very inclined EAS induced by cosmic rays. Discrimination between signal and background is based on the balance of the total electromagnetic and total muonic signal on the ground.

We demonstrate that a km^2-scale wide-field ground-based gamma-ray observatory is predicted to be capable of detecting VHE atmospheric and astrophysical neutrinos at an average rate of $2.09 \times 10^{-1}\ yr^{-1}$, or ~ 1 event every 5 years. The highest estimated event rate is $3.72 \times 10^{-1}\ yr^{-1}$ or ~ 1 event every $2-3$ years.

Keywords: Astrophysical Neutrinos; Atmospheric Neutrinos; Gamma rays; Cosmic rays; Gamma-Ray Ground Observatories

Contents

List of Figures

List of Tables

Acronym List

AGN	Active Galactic Nuclei
AIRES	AIR-shower Extended Simulations
a.s.l.	Above Sea Level
CC	Charged Current
CMB	Cosmic Microwave Background
CORSIKA	COsmic Ray SImulations for KAscade
CR	Cosmic Ray
DOM	Digital Optical Module
FoV	Field of View
IACT	Imaging Atmospheric Cherenkov Telescope
LPM	Landau-Pomeranchuk-Migdal
NC	Neutral Current
PMT	PhotoMultiplier Tube
SWGO	Southern Wide-field Gamma-ray Observatory
UHE	Ultra High Energy
UHECR	Ultra High Energy Cosmic Ray
VHE	Very High Energy
WCD	Water Cherenkov Detector

Chapter 1

Introduction

Astroparticle multi-messenger physics combines information pertaining to a single phenomenon extracted from different messengers, namely electromagnetic radiation, gravitational waves, neutrinos, and cosmic rays. As each messenger is created by different astrophysical processes, they reveal different information about their sources. This approach has the potential to address fundamental problems, such as those related to physics in extreme phenomena, the long-standing question on the origin of UHECRs, the nature of dark matter, the possibility of a Lorentz invariance violation and even the existence of previously undiscovered particles. There are numerous experiments that resort to EAS detector arrays to study gamma rays with very-high energies. With this thesis, we aim to determine whether such experimental setups are capable of neutrino detection, thus possibly allowing for multi-messenger observations. To achieve this, we carry out a study of the sensitivity of a ground-based gamma-ray observatory to neutrinos with energies ranging from 100 TeV to 1 PeV. Ensuing calculations take into consideration the currently proposed SWGO design and its expected performance.

Given the layout of an EAS detector array, direct neutrino detection within a given station is not a viable approach. Instead, this work focuses on the possibility of measuring these neutrinos by studying the extensive air showers generated by the interaction of these particles with the atmosphere. Neutrinos exhibit very small cross sections and very large mean free paths, thus the showers they induce are capable of having distinguishable signatures. These include events with a single active station with very high signal, as the neutrino interacts very close to the array and deposits a large amount of energy in the nearest station. Another possible signature is that of very inclined showers produced close to the ground. These are the events that will be considered as the sources of signal, while background will be attributed to extensive air showers induced by cosmic rays under similar circumstances.

Hence, this thesis is organised as follows: in section 2, we provide a brief introduction to extensive air showers, neutrinos, the showers they may induce, and how neutrino detection is typically approached. This is followed by a description of the current experimental panorama, regarding gamma-ray and astrophysical neutrino observatories in section 3. In section 4 we detail the workflow established for the sensitivity computation, and the programs employed at each step. This entails the simulation of extensive air showers, the detector response, and the extraction of relevant information from the simulated showers.

The results pertaining to background elimination, the estimation of the neutrino event rate and the impact of the signal resolution on the proposed measurement are discussed in section 5. This also accompanied by a study of the possibility of using up-going neutrinos as an additional contribution to the expected event rate. Finally, some conclusions are drawn in section 6.

Part I

Theoretical Introduction

Chapter 2

Main Focus of Thesis

2.1 Neutrinos

Neutrinos, commonly denoted by the Greek letter ν, are fermions (elementary particles with spin $1/2$) that interact with matter via the weak nuclear force and gravity. They are electrically neutral particles, whose rest mass is very small, much smaller than the remaining known elementary particles except for photons and gluons, which are devoid of mass. The masses of neutrinos are so small (the summed masses of the three types of neutrinos is smaller than $\sim 0.12 - 0.26\,\text{eV}$ [75]) it was long assumed that neutrinos were massless.

Of the two means through which neutrinos interact, the weak force has a very short range, while the gravitational interaction is extremely weak in the scale of individual particles, which is further compounded by the low rest mass of neutrinos. As a consequence, neutrinos have an extremely small cross section, commonly passing through matter unimpeded, thus also being very difficult to detect.

The two types of weak interaction neutrinos engage in are neutral and charged current interactions. Neutral current interactions are mediated by the Z boson, an exchange particle which does not carry any electrical charge, hence the designation of these interactions. The exchange of a Z boson leads to a transfer of momentum, spin and energy, but other properties such as charge and flavor remain unaffected. This means that a neutrino that interacts via neutral current is essentially undergoing a transfer of momentum and energy with a ”target” particle, and the resulting particle is still a neutrino of the same flavor.

Charged current interactions are mediated by the W^+ and W^- bosons characterised by a positive and a negative electric charge, respectively. During these interactions, the W boson may induce the emission or absorption of an electron (or positron). It may also change the flavor of a quark and its electric charge, as is the case in a β decay or a K-capture. A high-energy neutrino that undergoes this kind of interaction is transformed into its partner lepton (electron, muon or tau). Examples of these interactions are shown in Figure 2.1. Should the neutrino not have sufficient energy to generate it’s partner’s mass, a charged current interaction cannot take place.

2.1.1 VHE Neutrinos

Very-High Energy (VHE; $E_\nu \sim$ PeV) neutrinos may be produced by the decay of secondary particles (such as very energetic muons[23] or charmed particles [57, 22]) originating from the collisions of cosmic rays (typically protons and heavier nuclei) with nuclei in the upper atmosphere. These cases are commonly referred to as atmospheric neutrinos. The interaction of cosmic rays with the atmosphere may produce charged pions that rapidly decay into muons and muon anti-neutrinos (or anti-muons and muon neutrinos). The muons resulting from the decay of pions are also susceptible to decay into an electron, electron anti-neutrino, and muon neutrino. As such, roughly two-thirds of atmospheric neutrinos are muon neutrinos and anti-neutrinos, and the remainder are electron neutrinos and anti-neutrinos.

Under these conditions, neutrinos typically exhibit energies in the range $10^7 - 10^{14}$ eV (10 MeV – 100 TeV) [35]. Some of the interactions which may produce these neutrinos are depicted in the Feynman diagrams of Figure 2.1. Given their origin, the flux of atmospheric neutrinos has a direct correlation with the flux of cosmic rays. For energies below $\sim$ 100 TeV – 1 PeV, the flux of atmospheric neutrinos is the main contributor to the neutrino energy spectrum, as can be seen in Figure 2.2. As the energy increases, the flux of cosmic rays decreases significantly, causing the contribution of atmospheric neutrinos to diminish. At higher energies, the flux of neutrinos originating from astrophysical sources exceeds that of atmospheric neutrinos.

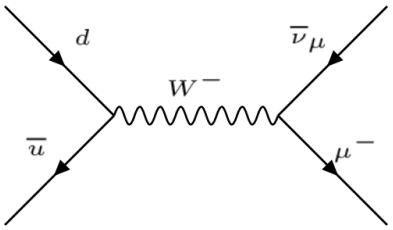

(a) Feynman diagram depicting the of decay of a pion (π^- : $d\overline{u}$) into a muon and a muon anti-neutrino.

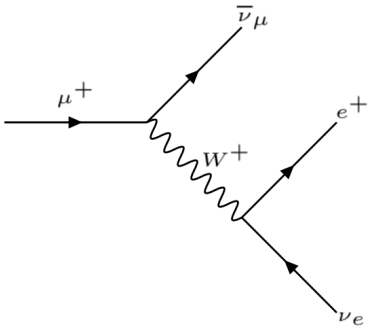

(b) Feynman diagram depicting the of decay of an anti-muon into a positron, electron neutrino, and muon neutrino.

Figure 2.1: Feynman diagrams depicting possible means of atmospheric neutrino production. Both cases occur via charged current interactions.

Within astrophysical objects such AGN [65, 67], the decay of charged pions resulting from the interaction of charged cosmic rays with radiation and/or molecular clouds leads to the production of neutrinos. Other potential sources of astrophysical neutrinos include galaxy clusters [71], starburst galaxies [18] and GRBs [**NusFromGRB**, 70]. Neutrinos originating from these sites are, at least in theory, capable of exhibiting energies up to 10^{18} eV (1 EeV) [66], although none has ever been observed above 10 PeV. These VHE and Ultra-High Energy (UHE, $E_\nu \sim$ EeV) particles can travel long distances without being absorbed, as would be the case for high-energy photons, or deflected by magnetic fields, as they are devoid of electric charge. Except for redshift energy losses and flavour oscillations, VHE and UHE astrophysical neutrinos remain unmodified as they traverse the cosmos. Thus, they are unique tracers of cosmic-ray acceleration

and point directly to their sources. They also provide a unique probe into the high-energy phenomena that stand at their origin, allowing for otherwise inaccessible tests of particle and fundamental physics. However, their detection is a difficult task.

Within the aforementioned high-energy phenomena, VHE protons produce pions via interactions with photons or proton-proton inelastic collisions. The decay of these pions produces gamma rays (in the case of π^0), or leptons and neutrinos (in the case of $\pi^{\pm}$). Given this, neutrinos are often taken as an indicator of hadronic acceleration, making them useful in the study of astrophysical jet composition and possible connections to UHECRs [39]. One recent example of this is the detection, by the IceCube Neutrino Observatory, of neutrinos spatially coincident with the BL Lac-type blazar TXS 0506+056 as it was undergoing a gamma-ray flare [28], providing one of the clearest signals yet that astrophysical jets accelerate hadrons to very high energies. This observation effectively confirms that AGN are among the potential sources of astrophysical neutrinos. VHE neutrinos may also result from the decay of heavier particles produced in the interaction of cosmic rays with the CMB (Cosmic Microwave Background) and other background radiations [73, 38].

Given the possibility of both atmospheric and astrophysical neutrinos to attain considerable energies, these particles are capable of inducing extensive air showers by interacting with the Earth's atmosphere, which can then be used to study the properties of neutrinos in such energy ranges.

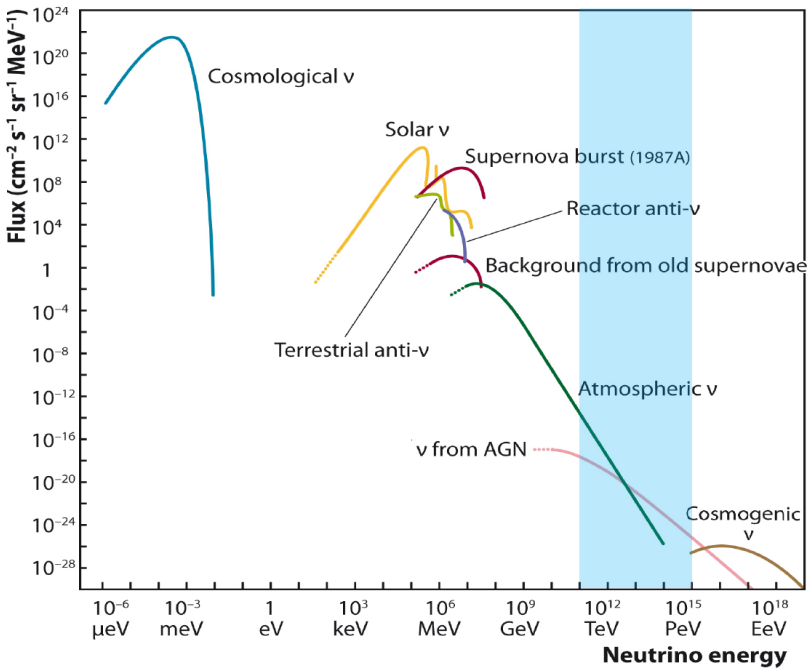

Figure 2.2: Neutrino energy spectrum, taken from [47]. IceCube focuses on the range of energies 10^{14} – 10^{16} eV, the Pierre Auger Observatory on energies of the order of 10^{18} eV and above, while the SWGO would work in the 10^{11} – 10^{15} eV range, as highlighted in blue.

2.2 Extensive Air Showers

When a very energetic particle (the primary particle) enters the atmosphere and interacts with the nucleons of the atoms, new (secondary) particles are produced, among which the energy of the primary particle is divided. Interactions of these particles lead to the production of new particles, a process which is repeated successively, generating an extensive air shower which may reach the Earth's surface. When a cascade of particles is initiated by the interaction of a hadronic particle, it is possible to distinguish four main components according to the different types of particles and their respective penetrating power:

- Electromagnetic (EM): Made up of electrons, positrons and photons produced from the fast decay of neutral pions (π^0). It constitutes the majority of the extensive air shower, carrying over 90% of its energy. This component is more thoroughly analysed in section 2.2.1;
- Hadronic: close to the shower core, composed predominantly by charged pions and fast baryons. Further details pertaining to this component are provided in section 2.2.2;
- Muonic: muons (and anti-muons) that arise mainly from the decays of charged pions ($\pi^{\pm}$). Most of these particles travel far enough to reach the Earth's surface. Section 2.2.3 provides a more detailed description of this component;
- Neutrinos: Muon production and decay in the atmosphere also results in the production of atmospheric neutrinos of energies $\lesssim 100\,\mathrm{TeV} - 1\,\mathrm{PeV}$. However, these neutral particles are very unlikely to interact with the atmosphere, thus the energy they carry is essentially undetectable, except for the rare occasion when they do interact before reaching the ground.

2.2.1 Electromagnetic Component

The first component to be analysed is the electromagnetic one, whose development is largely similar to that of the shower induced by a photon. In particular, the processes that most significantly contribute to the development of this component are e^+e^- pair creation and bremsstrahlung, two processes that exhibit a similar radiation length as shown in equation 2.1.

$$X_0\big|_{\mathrm{brem}} \approx 0.78\, X_0\big|_{\mathrm{pair}} \tag{2.1}$$

where X_0 is approximately $37\,\mathrm{g\,cm^{-2}}$ in air.

As the shower develops further within the atmosphere, energy losses via ionisation become progressively more important. Resorting to a simple model, it is then possible to attempt to infer some of the attributes of the electromagnetic shower.

Heitler Model

To obtain the most general features of an electromagnetic cascade, a toy model is sufficient. Such a description was first achieved by Heitler [42], who described a shower consisting solely of particles of

the same type that interact at a length[1] $\lambda = X_0 \ln 2$. Each interaction would give rise to two new particles, among which the energy of the initial particle would be equally divided. As a consequence, the number of particles doubles at each step, meaning that after N steps the cascade would have covered a length of $X = N\lambda$ and would be made up of 2^N particles, as depicted in Figure 2.3. At a given level n, each particle would have an energy of $E_n = E_0/2^n$, where E_0 denotes the energy of the primary particle.

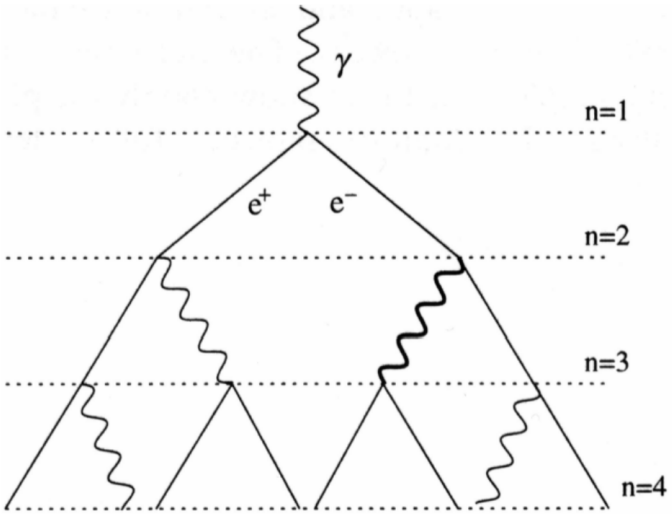

Figure 2.3: Heitler model for an electromagnetic shower. Figure taken from [7].

This process is repeated until the particles produced reach a critical energy, E_c, below which the interaction cross section would be zero, and no further interactions can take place. In air, this critical energy is roughly 85 MeV, and it corresponds to the point where losses of energy by ionisation are comparable to the losses via bremsstrahlung, as expressed by equation 2.2.

$$\left.\frac{dE}{dX}\right|^{ion}_{E=E_c} = \left.\frac{dE}{dX}\right|^{brem}_{E=E_c} \tag{2.2}$$

After this point is reached, energy loss occurs exclusively through ionisation processes (collisional energy loss) and the number of particles within the shower stops increasing. As such, each cascade is also characterised by a maximum number of particles, as given by equation 2.3, which is reached at a depth of X_{max} as shown in equation 2.4.

$$N_{max} = \frac{E_0}{E_c} \tag{2.3}$$

$$X_{max} = X_0 \ln\left(\frac{E_0}{E_c}\right) \propto \ln E_0 \tag{2.4}$$

Based on equation 2.4, it is evident that the shower maximum depth exhibits a logarithmic dependence with the primary energy, E_0.

Even taking into account the crude nature of the assumptions of the Heitler model, the behaviour outlined by equations 2.3 and 2.4 does adequately described what is observed in data and in complex

[1] More accurately, λ denotes the distance, in grammage, over which an electron loses, on average, half of its energy via radiation

Monte Carlo simulations. Overall, this is the case for energies up to $E_0 = 10^{17}$ eV, after which the discrepancies between the data and predicted behaviour start becoming significant. This can be attributed, in part, to photon showers becoming more deeply penetrating at higher energies. In turn, this change in behaviour can be, in part, explained by the appearance of small hadronic showers during the development of the electromagnetic cascade through the atmosphere. To further compound the issue, at around $E_0 = 10^{19}$ eV an additional factor is introduced: the Landau-Pomeranchuk-Migdal effect [54, 25], otherwise referred to as the LPM effect. At high energies or high matter densities, this effects predicts a reduction of the cross section of both bremsstrahlung and pair production as a consequence of the interference from successive scattering centres. At even higher energies, photons reaching the Earth can interact with its magnetic field via pair production, beginning the development of the shower earlier and thus also leading to a smaller average value of X_{max} of these photon showers.

2.2.2 Hadronic Component

In the case of showers induced by either a proton or an iron nuclei (or any other in between), hadronic interactions must be taken into account. As was the case with electromagnetic showers, a toy model is sufficient to obtain the general features of showers with an hadronic component. This model is henceforth referred to as the hadronic Heitler model[2], as it is based on the same principles.

Hadronic Heitler Model

Making use of the same principles described in section 2.2.1, it is possible to put together a toy model that accounts for hadronic interactions [53]. The development considered for hadronic showers in the present model is depicted in Figure 2.4, where an hadronic particle can be seen interacting with the air molecules, thus producing N_{mult} particles. More specifically, for the model being considered the particles resulting from the aforementioned interaction are exclusively pions, of which $2/3$ are charged ($\pi^{\pm}$) and the remaining $1/3$ are neutral (π^0).

The neutral pions, which are represented by dashed lines in Figure 2.4 do not re-interact with the atmosphere, yet such particles quickly decay through the $\pi^0 \rightarrow \gamma\gamma$ channel, except for at $E >$ EeV. The photons produced via this decay then lead to the generation of electromagnetic sub-showers.

In turn, the charged pions are expected to undergo hadronic interaction every length $\lambda_I = X_I \ln(2)$, where $X_I \approx 120\,\mathrm{g\,cm^{-2}}$ for pions in air. This process will continue while the energy of these pions remains above E_c^I, corresponding to the point at which the decay probability exceeds the probability of interacting. Once E_c^I is reached, the charged pions are assumed to decay into muons.

As was mentioned previously, the value of E_c^I for charged pions is dependent on the balance between interaction and decay and, as such, it also depends on the atmospheric density and pion decay length (which also depends on the energy of the pion). For the present case, E_c^I can be approximated to be 20 GeV [14].

[2]Sometimes also referred to as the Heitler-Matthews model.

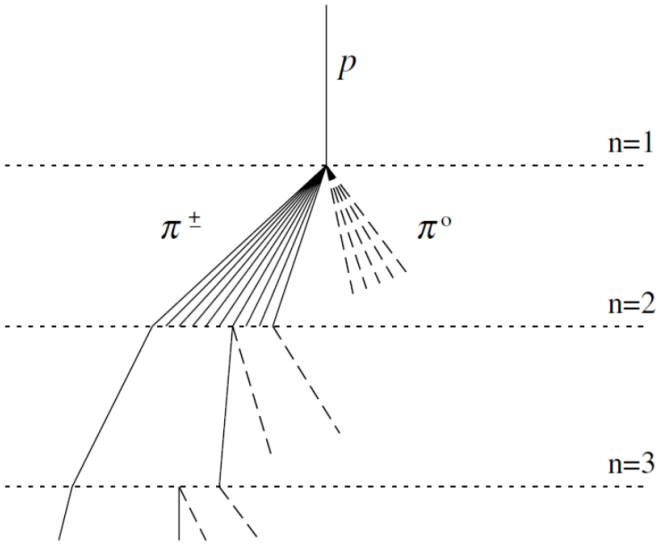

Figure 2.4: Schematic representation of an hadronic shower. Dashed lines represent π^0 while full lines represent charged pions ($\pi^{\pm}$). Not all pion lines are depicted after the $n = 2$ level. Figure taken from [53]

Having established this simple model, it is now possible to obtain a relation between the number of muons, N_μ, and the primary energy, E_0. In particular, the number of muons produced in a given shower is directly related to the number of pions resulting in equation 2.5

$$N_\mu = N_{\pi^\pm} = \left(\frac{2}{3}N_{mult}\right)^{n_c} = \left(\frac{E_0}{E_c^I}\right)^{\beta} \tag{2.5}$$

with,

$$n_c = \frac{1}{\ln(N_{mult})}\ln\left(\frac{E_0}{E_c^I}\right) \tag{2.6}$$

In the present model, the β parameter is given by equation 2.7

$$\beta = \frac{\ln\left(N_{mult}\right)}{\ln\left(\frac{2}{3}N_{mult}\right)} \tag{2.7}$$

If the average hadronic interactions multiplicity is assumed to range from $N_{mult} = 10$ to $N_{mult} = 100$, and these values are applied to equation 2.7, one obtains $\beta \approx 0.9$. This value is similar to the one obtained by detailed air shower codes and constitutes one of the most sensitive variables to test hadronic interaction models.

Similarly to what was done in section 2.2.1, it is also possible to derive the depth of the shower maximum, X_{max} in a hadronic shower. To allow for the comparison of the X_{max} results of a photon induced shower with an hadronic one, only the electromagnetic component is taken into account to produce the shower longitudinal profile. As such, the X_{max} is closely related to the maximum of neutral pion production, and its value can be determined via equation 2.8.

$$X_{max} = X_s + X_0 \ln\left(\frac{E_0}{N_{mult} E_c}\right) \tag{2.8}$$

where E_c denotes the electromagnetic critical energy (as defined in section 2.2.1) and X_s is the depth of the first interaction. By comparing equations 2.4 and 2.8, it is evident that X_{max} depends on the primary energy in both cases, but an additional dependency on the average hadronic interactions multiplicity is also present in the latter case. As such, photon-induced showers are expected to have a higher penetration power than those induced by hadrons.

In addition to this, when accounting for the superposition model, which considers an iron nuclei induced shower to be equal to 56 proton showers with energy $E_0/56$, an additional modification can be introduced to equation 2.8, resulting in equation 2.9, which allows for comparisons between proton and iron showers,

$$X_{max} = X_s + X_0 \ln\left(\frac{E_0/A}{N_{mult} E_c}\right) \propto \ln\left(\frac{E_0}{A}\right). \tag{2.9}$$

Based on equation 2.9, proton showers are more deeply penetrating than iron showers, mainly because X_s is smaller for iron nuclei than for protons, but also since the logarithmic term is smaller for iron nuclei ($A = 56$). For the case of showers induced by heavy nuclei, the number of muons is given by equation 2.10

$$N_\mu = A\left(\frac{E_0}{A E_c^I}\right)^\beta = A^{1-\beta}\left(\frac{E_0}{E_c^I}\right)^\beta \tag{2.10}$$

While the model described is capable of reproducing the main dependencies and behaviour of N_μ and X_{max} in hadronic showers, it neglects a crucial aspect of hadronic interactions - the inelasticity. This hadronic interaction parameter, associated with the fraction of energy carried by the fastest particle, may lead to significant increases in X_{max} and decreases in N_μ in relation to the predictions of this simple model [53]. Regardless, this approach is sufficient to gain some insight into the sensitivity of N_μ and X_{max} to the shower parameters, mainly energy and primary mass.

2.2.3 Muonic Component

The majority of muons within an extensive air shower can be attributed to the decay of unstable mesons, such as charged pions and kaons produced in hadronic interactions. Given that muons exhibit a small cross section and high survival time, caused by the large boost (above a few GeV), the majority of these particles are capable of reaching the Earth's surface and even penetrate a few meters into the ground.

This behaviour makes these particles an important tool to probe the hadronic interactions at very high energies, since an increase in the collision multiplicity or in the cross section of the secondary hadronic particles has a noticeable effect on the number of mesons produced, and consequently it also affects the number and energy spectrum of muons. Furthermore, as the properties of the muons also depend, even if indirectly, on the number of hadronic collisions, they can be used as a primary mass composition variable.

In addition to the aforementioned properties, muons also have a low presence in exclusively electromagnetic cascades, which allows one to distinguish showers induced by hadrons from those induced by

photons.

Moreover, a by-product of both muon production and decay are neutrinos. These are very hard particles to detect, thus being responsible for the majority of the undetectable energy in an extensive air shower.

2.3 Neutrino-Induced Showers

In the vast majority of extensive air shower array experiments, it is not possible to distinguish between vertical neutrino-induced showers and ordinary cosmic-ray-induced showers, as they exhibit very similar signatures. However, in the case of very inclined showers (roughly $\theta > 70°$) this discrimination becomes viable since there is a much larger grammage between the first interaction point and the ground. As a consequence, a proton typically induces a shower long before reaching considerable depths within the atmosphere. This leads to its electromagnetic component being completely absorbed early in its path, thus not reaching the detector array. The final result is a shower front at the ground level that is dominated by muons, which in turn induce sharp time traces in charged particle detectors, such as the water Cherenkov stations of an air shower array [48].

In contrast, neutrinos are capable of traversing large grammages before interacting. This means that showers induced by down-going neutrinos at large zenith angles may only begin developing much deeper in the atmosphere, producing traces that spread over longer times [55]. This is the strategy employed by, for instance, the Pierre Auger Observatory to look for neutrino-induced showers. It must be noted that the likelihood of a neutrino interacting is still markedly small, and the property that is being exploited in this scenario is that the probability of an interaction taking place remains essentially unchanged by the grammage traversed by an incoming neutrino.

There is also the possibility of showers being induced by up-going neutrinos. Most commonly, this occurs via the Earth-skimming mechanism, which entails a neutrino interacting in the Earth's crust, producing a lepton that generates a shower that can be detected, as depicted in Figure 2.5. Evidently, these contributions can only be accounted for should this process occur in close proximity to the array.

In the case of the SWGO, measurements are performed in the $10^{11} - 10^{15}$ eV range. This region is of particular interest as it allows for the study of both atmospheric neutrinos and astrophysical neutrinos.

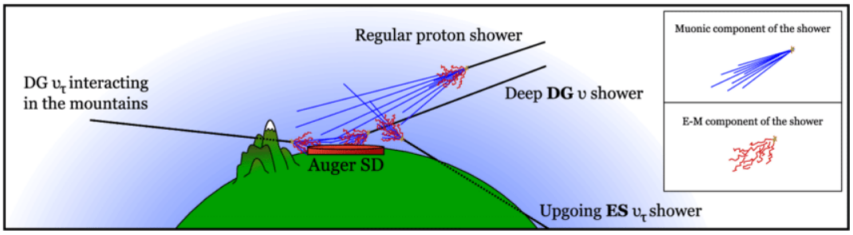

Figure 2.5: Diagram depicting the possible circumstances under which neutrino-induced showers and cosmic-ray-induced showers can be adequately distinguished. ES: Earth Skimming, DG: Down Going, SD: Shower Detector. Taken from [8].

2.4 Neutrino Detection

The energy spectrum of neutrinos of interest to the present thesis spans from a few GeV corresponding to neutrinos produced via the interaction of cosmic rays with the Earth's atmosphere (atmospheric neutrinos), to the region of very high and ultra high energies associated with the production of neutrinos in astrophysical sources (astrophysical neutrinos). Outside the scope of this thesis, there are other cases of interest for particle and astroparticle physics, such as the solar neutrinos with energies typically below 10 MeV.

The vast majority of neutrino detectors are located underground (or underwater) to shield them from cosmic rays that would otherwise contribute to the background of such measurements. However, neutrino detection should also be possible to some extent on ground-based gamma-ray detectors (such as the planned SWGO), which is what the present thesis aims to demonstrate.

2.4.1 MeV Neutrinos

Detection of MeV neutrinos predominately relies on the detection of the products of induced β decays. Early setups used a solution of cadmium chloride in water alongside scintillation detectors. Incoming anti-neutrinos with energies exceeding the 1.8 MeV threshold scatter of protons in the water, in an inverse beta-decay interaction, producing positrons and neutrons. The positrons annihilate with electrons, generating pairs of photons which can be detected via the scintillators. The neutrons are captured by the cadmium nuclei resulting in the emission of gamma rays of roughly 8 MeV which are typically detected a few microseconds after the photons produced by a positron annihilation event.

Alternatively, a radiochemical chlorine detector consists of a tank filled with fluid containing a chlorine solution. Under these conditions, neutrinos are capable of converting a ^{37}Cl atom into one of ^{37}Ar via a charged current interaction. The energy threshold for this interaction is 0.814 MeV. Periodically, the argon atoms are counted as a means to measure the number of electron capture radioactive decays. The first solar neutrino detection was achieved using a setup of this kind, containing 470 metric tons of fluid and located in the former Homestake Mine near Lead, South Dakota. This was also the first measurement of the deficit of electron neutrinos from the Sun [16]. A similar detector design makes use of the $Ga \rightarrow Ge$ transition which is sensitive to lower-energy neutrinos, as it has a lower detection threshold of 0.233 MeV.

2.4.2 MeV and GeV Neutrinos

The most noteworthy results in the MeV to GeV neutrino energy spectrum in recent years can be attributed to Cherenkov-based neutrino detectors, such as the Super-Kamiokande [34], and the Sudbury Neutrino Observatory (SNO) [20]. The key underlying phenomenon of such detectors is Cherenkov radiation, which is produced whenever a charged particle is moving through a medium at a speed exceeding the speed of light in that medium. Cherenkov detectors contain large volumes of a clear material, commonly water or ice, and rely on PMTs (Photo Multiplier Tubes) to detect the Cherenkov radiation of charged particles travelling through the detector medium. Neutrinos are capable of interacting

with atomic nuclei to produce charged leptons. If this interaction occurs within a Cherenkov detector, the Cherenkov radiation emitted by such leptons can be used to infer information pertaining to the incident neutrinos (such as direction and energy).

2.4.3 Very-High-Energy Neutrinos

The biggest challenge pertaining to VHE (and UHE) neutrino detection is increasing the sensitivity of detectors to allow them to see a reasonable number of events, since the flux of neutrinos at these energies is expected to be lower than the photon flux [3].The most common means of addressing this issue is instrumenting very large volumes, typically making use of large amounts of water or ice as is the case of the Baikal Deep Underwater Neutrino Telescope (BDUNT) [21] and the IceCube Neutrino Observatory [5], respectively.

[3]The main mechanism behind neutrino production, the hadronic mechanism, is common to photons.

Chapter 3

Current Experimental Panorama

In this chapter, we aim to briefly present the panorama of experiments dedicated to the study of very high energy and ultra high energy neutrinos, the theme of this thesis. Moreover, the experimental panorama of very high energy gamma rays is also briefly discussed, as we intend to study the potential of a wide-field ($\sim km^2$) ground-based gamma-ray observatory to measure VHE neutrinos.

3.1 Astrophysical Neutrino Observatories

There is a wide range of ongoing experiments dedicated to the detection of astrophysical neutrinos, such as SNO [20] (no longer active, now refurbished for use in the SNO+ experiment [12]), Super-Kamiokande [34], ANTARES [43] and the IceCube Neutrino Observatory [5], all of which are water Cherenkov detectors (except for SNO+, which uses a liquid scintillator). However, as mentioned in the previous section, neutrino detection can also be achieved via scintillators (e.g.Cowan–Reines neutrino experiment [61] and KamLAND [32]) and radio-chemical methods (e.g. SAGE experiment [36] and GALLEX/GNO experiments [46]).

Among the experiments previously mentioned, the IceCube Neutrino Observatory has made several recent contributions at VHE. IceCube is a cubic-kilometre-sized neutrino detector, placed deep in the ice of the geographic South Pole, Antarctica between depths of 1450 m and 2450 m [5]. Particle detection is performed based on a set of 5160 digital optical modules (DOMs) attached to 86 cables, each equipped with 60 DOMs. Each DOM is composed of a glass pressure-resistant sphere containing a photomultiplier and additional electronics. This allows it to operate independently and produce digital signals that are sent to the surface along the aforementioned cables (Figure 3.1). Its contributions include the detection of neutrinos with energies of the order of PeV [27] for which jets from GRBs or AGN are possible sources. The data it has gathered over time has also allowed for a more detailed characterisation of the diffuse astrophysical electron and tau neutrino flux [51]. Additionally, IceCube detected neutrinos spatially coincident with the BL Lac-type blazar TXS 0506+056 as it was undergoing a gamma-ray flare [28]. This constitutes one of the clearest signals to date that jets accelerate hadrons to very high energies, and demonstrates the potential of multi-messenger observations for probing conditions in extra-galactic jets.

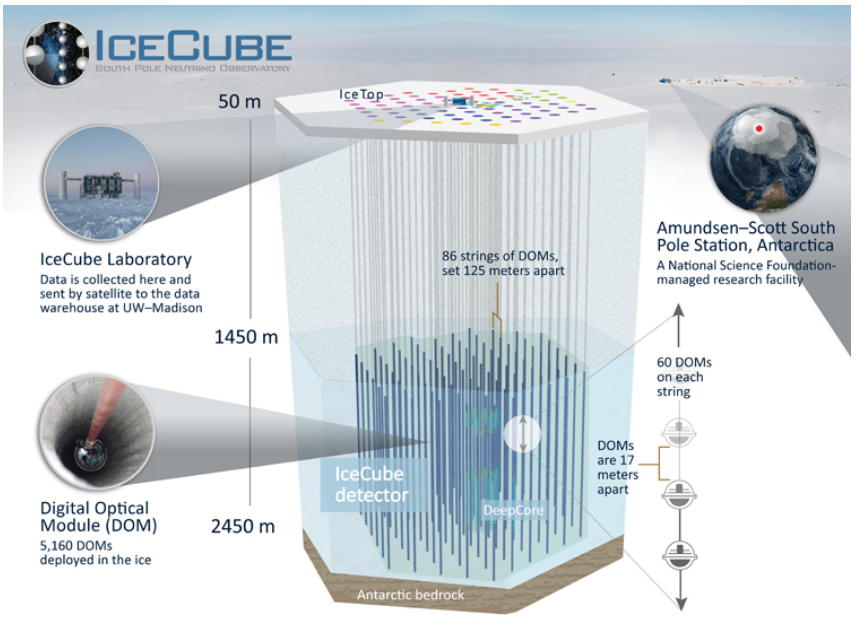

Figure 3.1: Schematic representation of the Icecube detector, taken from [45].

There is an experiment currently being carried out by the Pierre Auger Observatory that has the potential to detect astrophysical neutrinos. The Pierre Auger Observatory is a hybrid detector of cosmic rays of ultra-high energy located in Malargüe, Argentina [29]. It observes extensive atmospheric showers by resorting to both fluorescence telescopes and a ground array of water Cherenkov detection stations, as depicted in Figure 3.2. This setup covers an area of approximately $3000\,\mathrm{km}^2$, containing 1600 water Cherenkov detection stations arranged in a triangular pattern of $1.5\,\mathrm{km}$ side. Each of these surface stations is cylindrical in shape, with a $10\,\mathrm{m}^2$ base and $1.5\,\mathrm{m}$ height, containing 12 tons of water. The inside of these tanks is covered with a highly reflective material, and three PMTs are placed on the top of tank, that collect the Cherenkov light produced by charged particles crossing the station. This setup is complemented by 24 atmospheric fluorescence detector telescopes grouped into four locations, as can be seen in Figure 3.2. Due to its configuration, the Pierre Auger Observatory has the capability to observe rare showers induced by neutrinos with energies ranging from 100 PeV to 100 EeV [58, 55].

These showers are most efficiently identified if they are generated by neutrinos arriving at zenith angles above $\theta \sim 60°$ and interacting in the atmosphere in close proximity to the ground (down-going) [72]. They may also be products of the decay of a quasi-horizontal lepton emerging from the ground after an interaction of a neutrino within the Earth's crust (up-going) [15]. Both types of events produce an inclined shower that can be identified by the presence of a significant electromagnetic component alongside a broad time structure of signals in the water Cherenkov detectors. Despite these robust considerations and experimental setup, the Pierre Auger Observatory has not found any neutrino candidates to date. However, it has been capable of imposing stringent constraints on models of neutrino production at EeV energies [1, 2].

The aforementioned results from the Pierre Auger Observatory, together with upper limits from other experiments and expected neutrino fluxes for several models of neutrino production, are presented in Figure

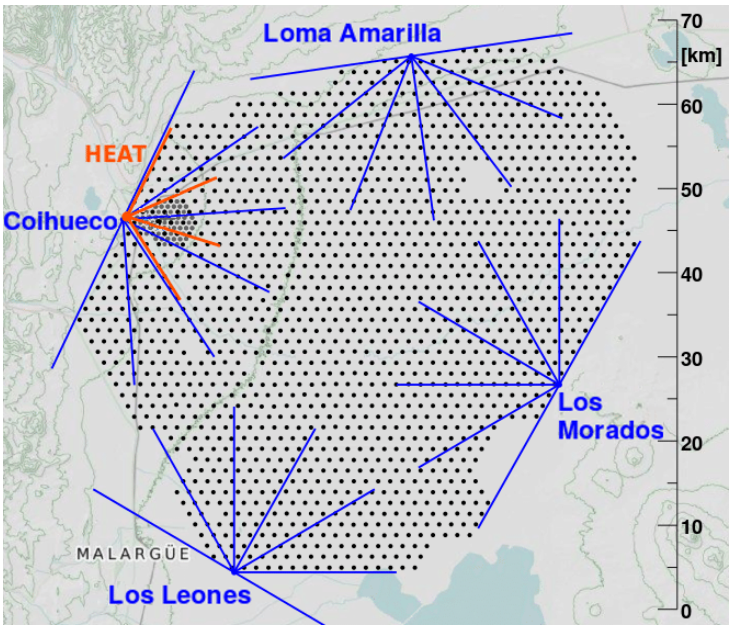

Figure 3.2: Schematic representation of the Pierre Auger Observatory. Each black dot is a water Cherenkov detector. Blue lines indicate the individual field of view of each fluorescence telescope. The field of view of the HEAT telescopes are indicated with red lines. Taken from [3].

3.3. It can be seen that the best sensitivity for the case of Auger is achieved at around 1 EeV. Furthermore, assuming a differential energy spectrum of the form E_ν^{-2} (the ν subscript refers to neutrinos), the Auger Collaboration derived a limit at 90% confidence level of $E_\nu^{-2}(dN_{\nu_\tau}/dE_\nu) < 4.4 \times 10^{-9}\,\mathrm{GeV\,cm^{-2}\,s^{-1}\,sr^{-1}}$ per flavour, in the energy range between 10^{17} and 2.5×10^{19} eV [4]. According to top-down models for ultra high-energy cosmic rays, a large flux of ultra high-energy neutrinos is expected. As shown in Figure 3.3, the conjugation of these models and the upper bounds of cosmogenic neutrinos achieved by the Auger Collaboration starts to constrain astrophysical models aiming to describe the UHECR flux suppression above 4×10^{19} eV due to energy losses of protons in the CMB.

The next generation of neutrino detectors is already in development, and includes projects such as SNO+ [12], Hyper-Kamiokande [59], IceCube-Gen2 [26] and KM3-Net [43]. These experiments seek to build on the experience of previous projects by either instrumenting larger volumes, refining the detection technology, or employing innovative means of neutrino detection.

3.2 Space and Ground-Based Gamma-Ray Observatories

High-energy gamma-ray detection is predominantly achieved via space-based instruments, as the absorption in the atmosphere precludes the products of the showers they generate from reaching ground-based detectors. The most notable detector within this category is the Fermi Large Area Telescope (Fermi-LAT) satellite. The observations performed by Fermi-LAT have led to the publication of four catalogues listing and categorising the AGN it has detected since it began operations in June 2008 (the latest catalogue covers data gathered between August 2008 and August 2016 [50]). It has also provided significant contributions to the field of gamma-ray astrophysics including the determination of

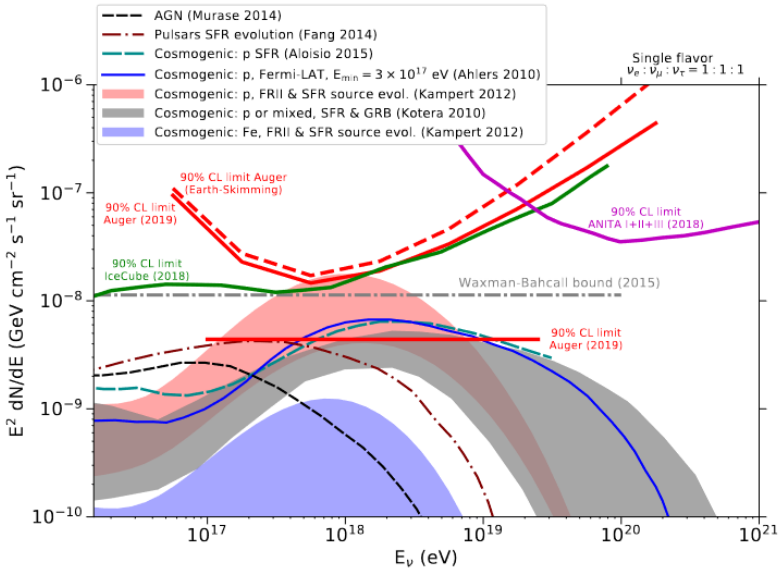

Figure 3.3: Upper limit at 90% C.L. to the normalisation constant k of the diffuse flux of UHE neutrinos $\phi_\nu = kE_\nu^{-2}$ based on data from the Pierre Auger Observatory (solid horizontal red line). The upper limits to the normalisation of the diffuse flux (differential limits) are represented by a solid red line (Auger, all channels and flavours) and a dashed red line (Auger Earth-skimming ν_τ only). The expected neutrino fluxes for several cosmogenic and astrophysical models of neutrino production are also plotted. All limits and fluxes are converted to a single flavour assuming a 1:1:1 ratio of the 3 neutrino flavours. Taken from [4].

the contribution of Fermi-2LAC blazars towards the diffuse TeV – PeV neutrino flux [52] as well as the observation of HE gamma rays towards the centre of the galaxy [49].

The detection of the extensive air showers generated by very-high-energy gamma rays falls primarily within the domain of ground-based observatories. These can be divided into two main classes: Cherenkov telescopes and EAS arrays. Cherenkov telescopes, also referred to as IACT (Imaging Atmospheric Cherenkov Telescopes), detect the Cherenkov radiation generated by the cascade of locally superluminal charged particles produced by the interaction of VHE gamma rays with the atmosphere. Cherenkov light is collected in a large reflecting surface then projected onto a camera placed in the focal plane of the reflector. These detectors typically have a high sensitivity and a low energy threshold, however common drawbacks include a low duty cycle (roughly 1000 – 1500 h/year) and small field-of-view (FoV) [11]. Several experiments resort to systems with multiple Cherenkov telescopes, as it allows for better background rejection, and a better energy and angular resolution than a single telescope. At the moment of writing, there are three notable IACTs in operation: MAGIC, HESS and VERITAS.

- The MAGIC (Major Atmospheric Gamma Imaging Cherenkov Telescopes) observatory, located in the Canary Island of La Palma, consists of two Imaging Atmospheric Cherenkov telescopes situated at about 2200 m above sea level [19].

- The HESS (High Energy Stereoscopic System) observatory located in Namibia is made up of five telescopes, four with a mirror 12 m in diameter, arranged in a square and 120 m apart from each other. The fifth telescope, placed in the centre of the array, is larger with a diameter of 28 m [37].

- The VERITAS (Very Energetic Radiation Imaging Telescope Array System) observatory situated near Tucson, Arizona, is a system of four telescopes, each with a diameter of 12 m [56].

Building on the technology of these current generation ground-based gamma-ray detectors, there is also the CTA (Cherenkov Telescope Array) project [63]. It aims to build an instrument capable of providing an order of magnitude improvement in sensitivity over existing observatories. The current design scenario includes the deployment of two arrays of IACTs: one at the Northern Hemisphere focused on the study of extragalactic objects at the lowest possible energies, and another at the Southern Hemisphere, aiming to cover the full energy range and concentrate on galactic sources.

Ground-based observatories may also be EAS detectors, consisting of large arrays of detectors sensitive to charged particles generated in atmospheric cascades, placed at high altitudes. Overall, these instruments have a high duty cycle and a large FoV, but a lower sensitivity and higher energy threshold when compared to IACTs[11]. Measurements performed by these detectors rely on the direct sampling of the aforementioned charged particles, which can be achieved by employing a sparse array of scintillator-based detection stations. This was the case for the Tibet-ASγ experiment (located at 4300 m above sea level to reduce the energy threshold) [74]. Alternatively, a compact array can be used to cover the ground allowing for the efficient collection of incoming charged particles, thus lowering the energy threshold. This method was employed in the ARGO-YBJ detector, consisting of a layer of RPCs (Resistive Plate Counters) covering an area of $6700\,\mathrm{m}^2$ [62]. A similar approach was taken by the MILAGRO observatory, which was a water Cherenkov EAS detector consisting of a $\sim 5,000\mathrm{m}^2$ pool with PMTs surrounded by an array of 175 instrumented water tanks [60].

The lowest energy threshold that can be achieved with EAS detectors falls in the $0.5 - 1$ TeV energy range [11], hence such instruments tend to focus on the detection of VHE and UHE gamma rays. However, at such energies fluxes are markedly small, requiring large surface areas for detection to be viable (of the order of $10^4\,\mathrm{m}^2$). To discriminate from the charged cosmic ray background, it is possible to employ muon detectors dedicated to hadron rejection. Otherwise, this discrimination must be based on the shape of the reconstructed shower. The direction of particles reaching the detector can be computed from the arrival times, with an angular resolution of $\sim 1^\circ$ [11]. The difference in arrival times at different stations of an array allows for the measurement of the direction of the primary particle. The shadow in the reconstructed directions caused by the moon can be used as a means to calibrate the angular resolution of the detector.

One notable VHE gamma-ray ground-based detector currently in operation is the HAWC (High Altitude Water Cherenkov) observatory located in Puebla, Mexico, at an altitude of 4100 m [69]. It is designed to reach an over one order of magnitude improvement in sensitivity over its predecessor, MILAGRO. HAWC consists of an array of 300 steel tanks 7.3 m wide by 5 m high, covering an area of approximately $22,000\,\mathrm{m}^2$. Each tank is filled with water and contains four PMTs responsible for the detection of the Cherenkov light produced by high-energy particles striking the water.

The current generation of EAS detectors has recently been extended in the Northern hemisphere by a hybrid detector named LHAASO (Large High Altitude Air Shower Obsertory). Its first phase is composed of three major components [17], as depicted in Figure 3.4:

- A $1\,\mathrm{km}^2$ array (LHAASO-KM2A) containing electromagnetic particle detectors (ED), each with an

area of $1\,\mathrm{m}^2$, overlapped with 1171 underground water Cherenkov detectors, each $36\,\mathrm{m}^2$ in size with 30 m spacing, for muon detection (MD). The central part of this array covers a circular area with a radius of 575 m with 4901 EDs (15 m spacing). The outer ring has a radius of 635 m and is instrumented with 294 EDs (30 m spacing).

- A $78,000\,\mathrm{m}^2$ compact surface water Cherenkov detector array (LHAASO-WCDA).
- 20 wide field-of-view air Cherenkov telescopes (LHAASO-WFCTA).

This setup is located at an altitude of 4,410 m above sea level in Daocheng, in the Garzê Tibetan Autonomous Prefecture in Sichuan, China. LHAASO has already found a dozen ultra-high-energy (UHE) cosmic accelerators within the Milky Way and detected photons with energies exceeding 1 PeV, including one at 1.4 PeV [24]. However, the Southern hemisphere remains largely devoid of any such instruments, despite the potential for the mapping of large-scale emission, as well as providing access to the full sky for transient and variable multi-wavelength and multi-messenger phenomena.

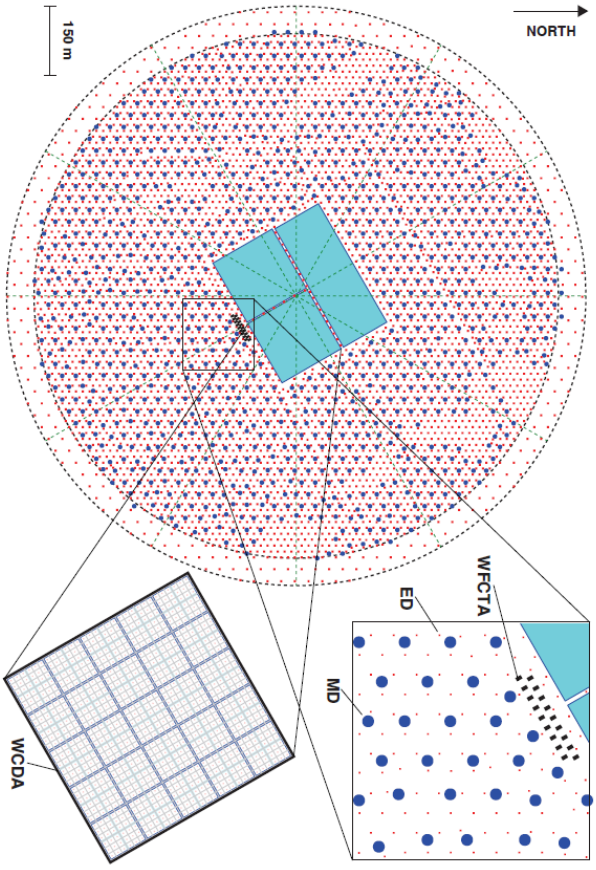

Figure 3.4: Layout of the LHAASO experiment. The insets show the details of one the water Cherenkov detector array (WCDA) ponds and of the $1\,\mathrm{km}^2$ array constituted by two overlapping arrays of electromagnetic particle detectors (ED) and of muon detectors (MD). The telescopes of the wide field-of-view air Cherenkov telescope array (WFCTA), located at the edge of a pond, are also shown. Taken from [17].

The SWGO (Southern Wide-field Gamma-ray Observatory) aims to fill this gap, as it will be the first high-altitude gamma-ray observatory to provide wide-field coverage of a large portion of the southern sky.

As such, it will complement current and future detectors, such as the aforementioned HAWC, LHAASO, and CTA. This detector is foreseen to be made up of a compact inner array spanning an area of 80 000 m^2, containing 4000 detection stations , surrounded by a sparser outer array of 1000 detection units, covering an area of 220 000 m^2 [9]. This proposed layout can be seen in Figure 3.5.

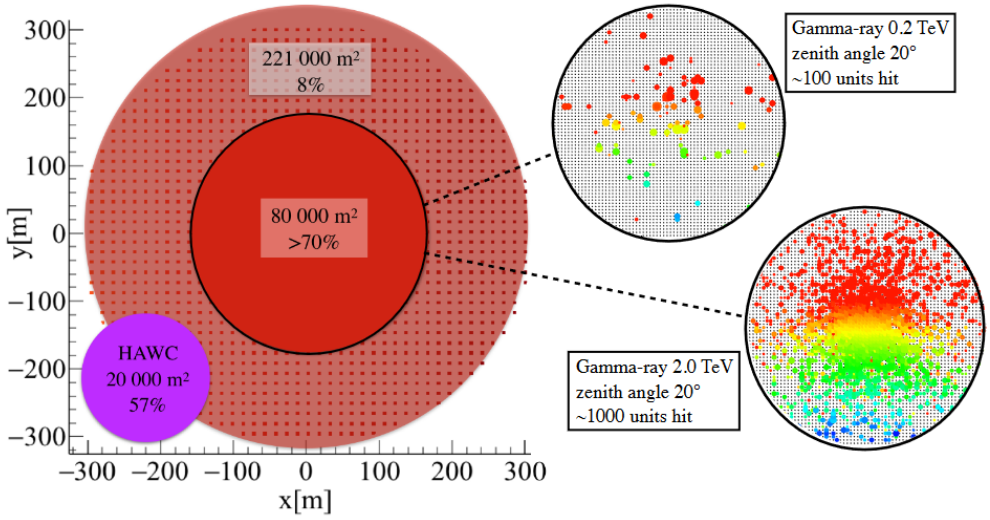

Figure 3.5: Left: Array configuration of the SWGO with instrumented areas and ground coverage indicated (HAWC equivalent for comparison). **Right:** SWGO response for two simulated gamma-ray events. The color coding denotes the time gradient. Taken from [9].

The design of the inner compact array part aims to drive the low-energy performance of the observatory, while the outer sparse array will extend the effective area to improve detection at higher energies. The dense inner array will cover roughly four times the area of the HAWC Observatory's main array, resulting in an increased flux sensitivity. The typical spread of particles for air showers with energies below 200 GeV is $\sim$ 75 m ($\sim$ 150 m) when induced by gamma rays (protons) [40]. Figure 3.5 shows the response of a simulated detector to a shower induced by a 200 GeV gamma ray. This illustrates the low particle density associated with these showers. Therefore, to effectively measure gamma rays with energies below 1 TeV it is paramount to employ a dense, large instrumented area.

In contrast, muons typically have significant transverse momentum due to which they reach the detector at a larger distance from the shower core. By increasing the muon-sensitive area, the identification of showers induced by hadronic particles is improved. This also reduces the background rate over the energy range of the observatory. The sparse outer array is a cost efficient means of increasing the effective area for high energy gamma rays. Particle densities for high energy showers reaching the sparse array are high enough that fewer active detector stations are required to accurately reconstruct the basic shower parameters. The dimensions of the outer array are projected to lead the observatory to possessing the highest point source sensitivity in the Southern hemisphere above tens of TeV.

The main constraints on site selection for the SWGO are: latitude between 10 and 40 degrees south, altitude higher than 4500 m, average yearly temperature above the freezing point of water, and adequate access to water sources. Numerous potentially suitable sites between 4800 and 5000 m in altitude have been identified, such as: the Atacama Large Millimeter/submillimeter Array (ALMA) site in the Atacama

Desert in Chile; the Cerro Vecar in Argentina where QUBIC and LLAMA are being built; the ALPACA site in Bolivia; and Laguna Sibinacocha, located in Peru [9].

Part II

Implementation & Results

Chapter 4

Implementation (Program Stack)

4.1 Shower Generation

The main program used to generate extensive air showers in this work is CORSIKA (COsmic Ray Simulations for KAscade) version 7.7410 [41]. When simulating showers induced by upward-going neutrinos, whose interactions took place in the Earth's crust (a medium which cannot be adequately reproduced using the aforementioned version of CORSIKA) a different program, AIRES [64] version 2.8.4a, was used.

CORSIKA allows for the specification of several parameters associated with an extensive air shower such as: the primary particle type, its energy, zenith angle (θ), vertical height or vertical depth of the point of the first interaction, the target of this first interaction and the number of showers per run.A few parameters remained unchanged or unaddressed in all simulations, namely: the azimuth angle (ϕ), which took a random value between -180° and 180°, the magnetic field, and the observation level, which was fixed at 5200m above sea level, corresponding to the altitude of one the sites being considered for SWGO. The same kinetic energy cuts and atmospheric model were used for all simulations performed via CORSIKA.

The signature of a neutrino-induced shower that we aim to investigate is a very inclined shower (θ in the range 60° to 88°) produced close to the ground (vertical height of first interaction up to 12000 m). These events allow for the minimisation of background induced by EAS generated by either cosmic rays or gamma rays since such particles would have to traverse 2 to 28 atmospheres (depending on θ) without interacting to reach the vicinity of the detector, which is a very unlikely occurrence. If these showers do reach the detector, they are likely to be "old" cascades that can be distinguished from the case of neutrino-induced showers. The electromagnetic component of these "old" showers will have been severely attenuated, essentially only leaving the muonic component of the cascade.

This thesis focuses exclusively on the detection of electron neutrinos. When these particles interact with the atmosphere, they generate an hadronic and an electromagnetic component. The latter constituent is an EM shower induced by the electron produced from the interaction of the corresponding neutrino. Upon reaching the ground, the cascade has undergone a substantial development allowing it to generate

a large footprint, facilitating its detection.

The interaction of a tau neutrino or a muon neutrino with the atmosphere also gives rise to an hadronic component. In the case of a muon neutrino, the other product of this interaction is a muon, which can penetrate the atmosphere and reach Earth's surface without generating a particle shower. As a result, very little or no signal is deposited in the array, and no footprint is produced, making detection unfeasible.

In contrast, a tau behaves similarly to a heavier version of the electron, and is more highly penetrating. Due to its mass, it is the only lepton that can decay into hadrons. The possibility of introducing an additional hadronic component means showers induced by tau neutrinos exhibit a more complex and erratic behaviour, although their detection is still viable. Because of this, the simplest case, corresponding to the electron neutrino, was chosen instead. Thus, the sources of signal are very-inclined showers induced by electron neutrinos with energies in the TeV and PeV range. Given these considerations, CORSIKA was used to generate 1000 showers for each of the following combination of parameters:

Neutrino-induced showers: setting electron neutrinos as primary particles, the following values were considered for each of CORSIKA's input parameters:

- Energy of primary particle: 100 TeV and 1 PeV;
- Zenith Angle (θ): 60°, 70°, 75°, 80° and 88°;
- Fixed Vertical Height of First Interaction (above observation level): 5, 10, 13, 20, 30, 50, 100, 250, 300, 350, 400, 450, 500, 800, 1000, 1200, 1500, 1700, 2000, 3000, 4000, 5000, 8000, 10000 and 12000 m. The maximum value of this particular parameter was fixed based on successive simulations, as larger values result in little change in the efficiency curves that are extracted from these simulations.

Proton-induced showers: Unlike neutrino-induced showers, the first interaction height is not fixed, but varied randomly according to the appropriate mean free path. The following values of input parameters were used:

- Energy of primary particle: 1 GeV, 10 GeV, 100 GeV, 1 TeV, 10 TeV, 100 TeV, 1 PeV, 10 PeV, 100 PeV, 1 EeV and 10 EeV;
- Zenith Angle (θ): 60°, 70°, 75°, 80° and 88°.

AIRES was used for the simulation of showers induced by up-going electron neutrinos interacting in the Earth's crust close to the detector array. This program does not include neutrinos as predefined primary particles, so they must be introduced via a so-called special particle file. To achieve this, CORSIKA is used to simulate 10000 vertical showers induced by 1 PeV electron neutrinos interacting at a vertical height of 19000 m. The observation level is placed 1m below this point, at 18999 m. The particles detected at this level are collected into a file detailing their id, energy and momentum components, which is used to generate a special particle. This is then used as a primary particle for simulations in AIRES. This special particle generation procedure is repeated every run, by randomly selecting a case out of the 10000 created.

The neutrino events to be considered in the AIRES simulations are those associated with very inclined showers, with the distinction that the primary particle is now travelling upwards. Given that the Earth's

crust has a much higher density than the atmosphere ($\approx$ 1000 times larger), showers develop and are attenuated in much shorter lengths, leading to the necessity of accounting for distances of a few meters (up to 5 m vertically) between the point of first interaction and the observation level. The Earth-skimming mechanism associated with up-going neutrino events is of particular relevance for the case of VHE and UHE neutrinos. Hence, within the context of the present study, the focus of the simulations is set on neutrinos with energies in the PeV range.

Accounting for the considerations listed above, AIRES was used to simulate 1000 showers induced by up-going electron neutrinos for each of the following set of parameters:

- Energy of Primary Particle: 1 PeV;
- Zenith Angle (θ): 92°, 100°, 105°, 110° and 120°
- Fixed Vertical Height of First Interaction (below ground level): 1, 2, 3, 5 and 10 m.

4.2 Detector Response

The amount of signal expected to be registered by a given station of the array when struck by a given particle was simulated with Geant4 [10]. The case study used in this work is the SWGO experiment [9], which is expected to rely on water Cherenkov detectors. In these simulations, we'll employ one of the candidate configurations for the stations of this observatory [30]. This base unit of the array was represented within Geant4 by a cylindrical tank filled with water, with a base radius of 2 m, height of 1.7 m, and 4 PMTs placed at the bottom, as depicted in Figure 4.2. The particle interactions occurring within the station were simulated via the *FTFP_BERT* physics list containing the default hadronic, electromagnetic and decay physics [13].

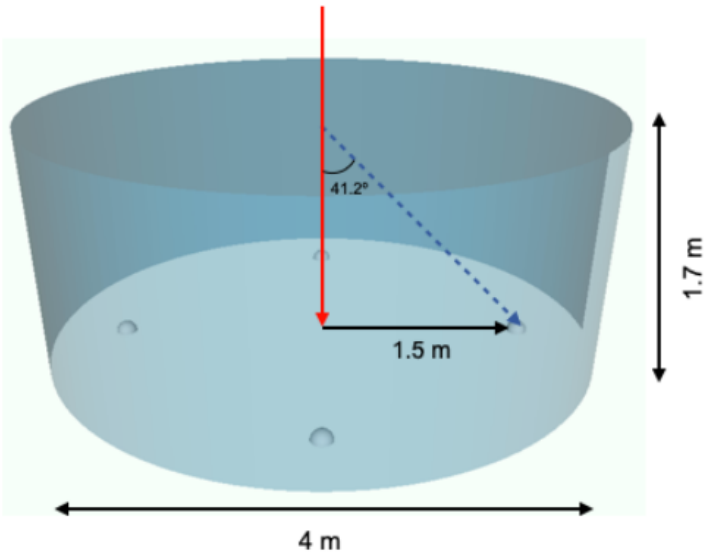

Figure 4.1: Water Cherenkov detector concept used in this study. The tank is filled with water,and 4 PMTs (Photo Multiplier Tubes) are placed at the bottom of the structure. Taken from [30].

Three types of particles were injected vertically into the Geant4 station recreation: electrons, muons and protons, to treat the electromagnetic, muonic and hadronic components of an extensive air shower, respectively. For each case, the kinetic energy of the injected particle assumed values ranging from 10 keV to 10 PeV, with 500 particles injected for each combination of energy and primary particle type. These simulations result in the calibration curves presented in Figures 4.3, 4.5 and 4.4, corresponding to the injection of electrons, muons and protons, respectively. These curves were parameterised, allowing to establish a correspondence between the energy of a particle contained within an extensive air shower and the signal it generates when it reaches a station of the array. Each of these sets of points was saved in individual ROOT files (.root), and then used by the shower parsing programs as a means to translate the energy reaching the stations of the array into signal.

Focusing on the EM calibration curve (Figure 4.3) at lower energies (roughly $E < 10^{10}$ eV), the signal produced grows at a near linear pace. As the energy increases, the signal produced within the station begins to saturate, with a maximum value likely to fall between $10^6 - 10^7$ p.e.. As there is no saturation of the PMT signal implemented in the detector simulations, the origin of this saturation is expected to be related to the leakage of the large electromagnetic shower produced in the station upon the particle entrance.

The hadronic component calibration curve (Figure 4.4) exhibits an increase in signal generation for energies up to 10^9 eV derived from the emission of Cherenkov radiation by increasingly energetic particles. At around 10^9 eV there is a change of slope indicating that the proton reaches $\beta \approx 1$ and the increase in signal comes essentially from the increase of number of shower particles produced by the interaction of the proton with the water atoms. The *FTFP_BERT* physics list is only capable of handling these inelastic hadron-nucleus processes for energies up to 100 TeV [13], hence the absence of points above $log_{10}(E/\text{eV}) > 14$.

Lastly, the calibration curve obtained for muons (Figure 4.5), which exhibits a noticeable increase in signal between the energies of 10^7 eVand roughly 10^9 eV, which is the result of the emission of Cherenkov light on behalf of a non-relativistic muon traversing the station. While the muon is non-relativistic, an increase in its energy also leads to an increase in signal. When a muon enters the relativistic regime, at around 10^9 eV, the emission of Cherenkov light reaches its limit leading to the plateau between 10^9 eV and 10^{12} eV. For larger energies, muon energy losses to ionisation may lead to the production of delta rays, which produce their own EM cascades, resulting in an increased signal generation. Regarding signal generation for energies below 10^6 eV, these events can likely be attributed to slow and very-slow moving muons that were stopped and decayed within the station, producing electrons of similar energy that then generate the small amount of signal registered. It must be noted that for the purposes of this work, it is sufficient to account only for the average detector response, while neglecting physical fluctuations and other effects, such as clipping particles.

Within the shower simulation frameworks, CORSIKA and AIRES, instead of considering a single station, a horizontal flat detector array is simulated. In this setup, each station is approximated by an area of 12.6 m^2 within the compact detector array, which spans a total circular surface area of 1 km^2, with a fill factor of 0.8. An example of the application of this setup is presented in Figure **??**. The choice of surface

area is derived from the already existing LHAASO observatory, which spans 1 km^2 with a fill factor of 0.04. Given this, future work will also need to evaluate the impact of using a sparser simulated array. For the calculations presented in this work, the height of the stations is neglected within the shower simulations, resulting in a 2D representation of the ground-based gamma-ray detector.

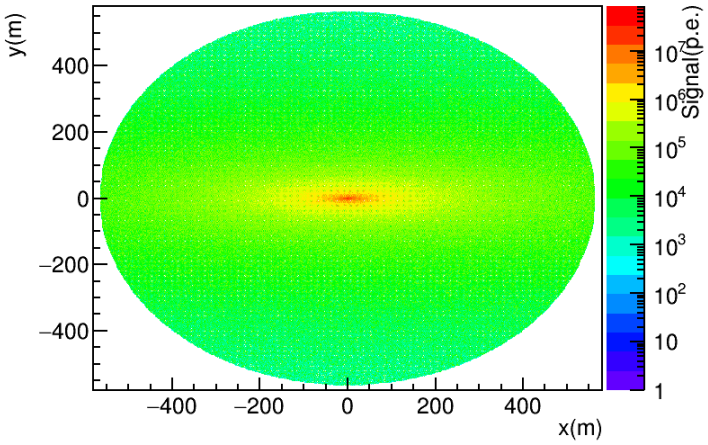

Figure 4.2: Water Cherenkov detector array used in this study. The array has an 80% fill factor and spans an area of 1 km^2, with each station being represented by an area of 12.6 m^2. This graph presents the cumulative footprint generated by 1000 very-inclined VHE proton-induced showers.

4.3 Shower File Parsing

For the purpose of extracting and saving information pertaining to the shower particles that reach the ground, two C++ codes were created: one to extract information from simulation files generated by CORSIKA, named CORSIKA_explorer, and another to do the same for files generated by AIRES, labelled Aires_reader.

CORSIKA_explorer reads the DAT files generated by CORSIKA during each run, from which it extracts the type and energy of the primary particle, the zenith angle and the height of first interaction (if it was fixed and not random). It also collects information regarding the energy, position , and type of particles reaching the ground. Using this information, the code also determines the energy deposited by the electromagnetic, muonic and hadronic components, and the total number of electromagnetic particles (electrons, positrons and photons), muons and hadrons. The signal is determined via the previously constructed calibration curves based on the energy and type of the particles arriving at the station, by applying ROOT's *Eval* method to the relevant curve. The *Eval* method computes a cubic spline interpolation between the two points closest to the point whose value is requested. If a value falls outside the graph range, a linear extrapolation is calculated instead.

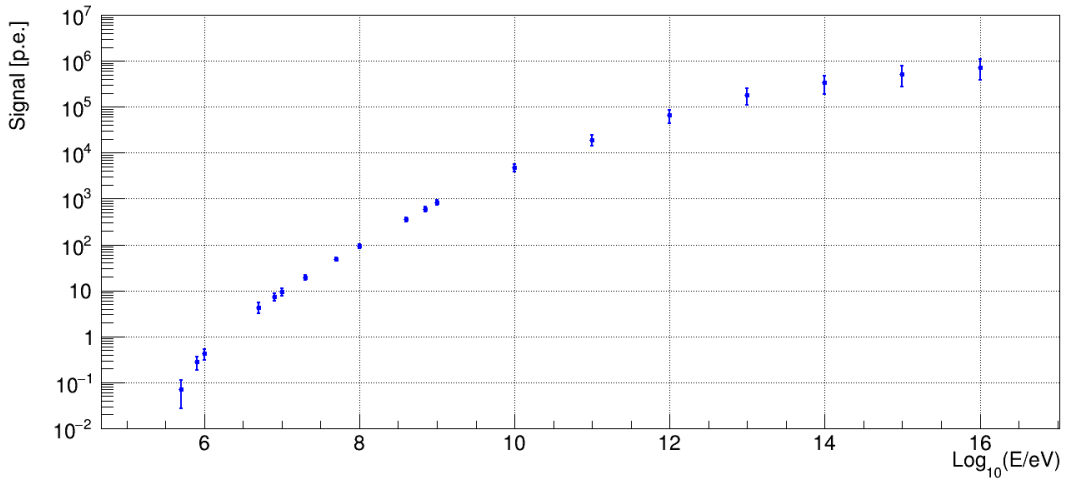

Figure 4.3: Calibration curve produced from the vertical injection of electrons, positrons and photons in the station depicted in Figure 4.2

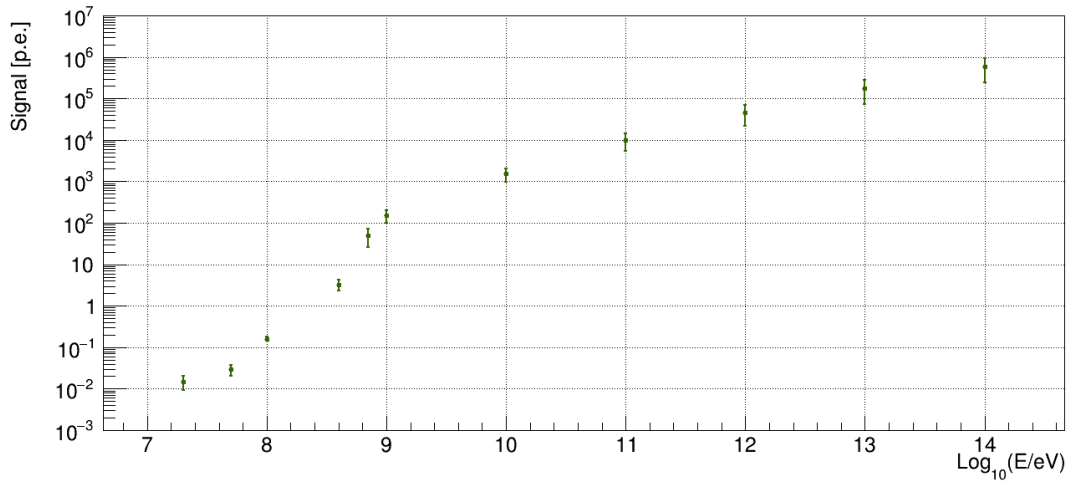

Figure 4.4: Calibration curve produced from the vertical injection of protons in the station depicted in Figure 4.2.

The Aires_reader program is used to determine the same quantities mentioned regarding CORSIKA_explorer. In this case, its input are .grdpcles files (instead of DAT files) that are generated by AIRES during each shower simulation which details the type, energy and position of the particles that reach the ground level.The full implementation can be summarised in the diagram presented in Figure 4.6.

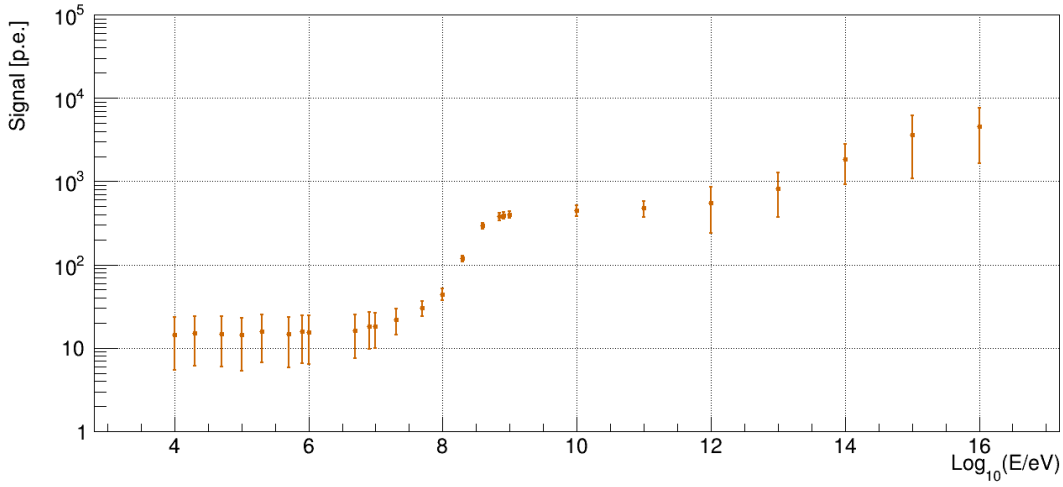

Figure 4.5: Calibration curve produced from the vertical injection of muons in the station depicted in Figure 4.2.

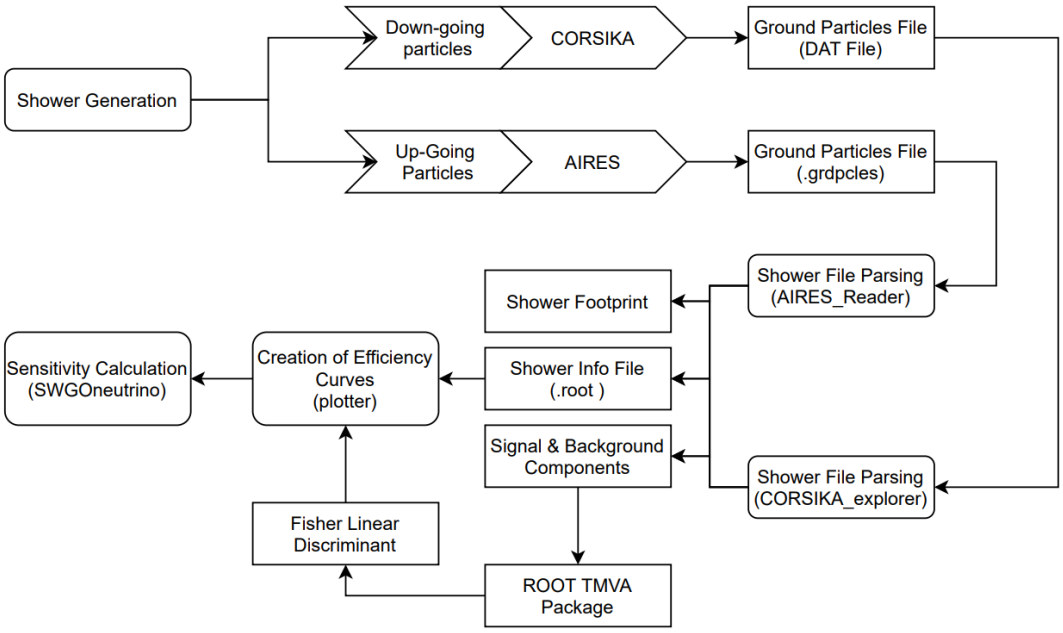

Figure 4.6: Flow chart depicting the steps, programs, code segments and files involved in the estimation of the sensitivity of an EAS array to neutrinos.

Chapter 5

Results

5.1 Neutrino and Proton-Induced Shower Discrimination

VHE Gamma-ray observatories such as LHAASO, or the projected SWGO, have to be capable of measuring the energy of an incoming shower and its muonic content. These two measurements are closely related to the total signal and the muonic signal, respectively, which are simulated quantities. The frameworks utilised in the simulation of showers, CORSIKA and AIRES, register all particles that reach the observation level and their properties. A detector is incapable of doing so, thus its approximated performance must be accounted for. This too, is achieved via the translation between the energy of a particle reaching the observation level and the signal that is generated in the station that it hits. In this work, we aim to determine whether these simulated parameters, that are closely related to those measured by gamma-ray observatories, can be used to distinguish between neutrino and proton induced-showers.

The key observables in discriminating between signal events induced by neutrinos and background events generated by cosmic rays are the electromagnetic signal (S_{em}) and muonic signal (S_{μ}) registered in the simulated WCD stations. These two quantities are calculated as described in chapter 4 based on the shower particles reaching the detector, their energy, and the parametrisations establishing the correspondence between energy and signal, as obtained from the calibrations curves (Figures 4.3-4.5).

This choice of variables is linked to the choice of very inclined showers as the signature of neutrino-induced showers. Since neutrinos are roughly equally likely to interact at any point in the atmosphere, they are also capable of producing showers in close proximity to the detector at steep incidence angles. In these cases, the electromagnetic component of the resulting showers is more pronounced (a larger S_{em} is produced) in relation to its muonic component. In contrast, showers induced by cosmic rays have their first interaction at much smaller grammages, thus the ensuing shower is older upon reaching the array, resulting in a more pronounced muonic component (a more significant value of S_{μ}) in relation to the electromagnetic one. This disparity is the principle we seek to exploit to distinguish signal from background. Showers induced by gamma rays are not included in background considerations as such cascades are dominated by an electromagnetic component that is significantly attenuated in the upper atmosphere. These showers are associated with moderately low values of S_{em} and S_{μ}, and are very likely

to be eliminated by the same cuts used to remove cosmic-ray-induced background. In addition, in the energy range which constitutes the focus of this work, the flux of gamma rays is considerably smaller than that of cosmic rays.

Proton-induced showers are grouped together as sources of background according to the zenithal angle at which they were injected, regardless of primary energy and height of first interaction. Neutrino-induced showers are taken as signal and grouped according to the zenithal angle, primary energy and vertical height of first interaction. These groups of points are outlined and stored in individual ROOT tree files (.root) via the CORSIKA_explorer C++ code.

Both data pertaining to signal and background is fed into ROOT's Toolkit for Multivariate Data Analysis (TMVA) [44] in order to separate the two classes of points via a Fisher discriminant. Fisher discriminant, more commonly referred to as Fisher linear discriminant analysis or just linear discriminant analysis (LDA), refers to a group of methods used in statistics, pattern recognition as well as machine learning to find a linear combination of features which separates two or more classes of objects. The result of this analysis may then be used as a linear classifier [33]. This discrimination process is applied to proton and neutrino-induced showers, for each fixed zenith angle. All proton-induced showers, regardless of energy, are taken as background, while only the cases of neutrino-induced showers with a given primary energy are taken as signal in the generation of the Fisher cut.

Besides this linear cut [1], an additional cut excluding all points with $\log_{10}(S_{em}) > 8.25$ is introduced for the cases with $\theta = 60°$ and $\theta = 70°$. This cut is added since such high values of electromagnetic signal are unlikely to be achieved by neutrino-induced showers in the energy range below ≈ 10 PeV, which contains most events expected in a detector such as the SWGO. The inclusion of such points would only further degrade the ability to distinguish neutrino and hadron-induced showers. An example containing both cuts is shown in Figure 5.1 for $\theta = 70°$.

Subsequently, since we are not aiming for a good separation between signal and background but instead a background free experiment, in such a way that any identification would be significant, the value of the normalisation of the Fisher cut is adjusted to the minimum value that achieves this. The efficiency of this final cut corresponds to the ratio of neutrino points located below the cut and the total number of neutrino points simulated with a given zenith angle and energy. Applying this cut to all values of fixed interaction depth of the neutrino-induced showers results in the discrimination efficiency curve of the respective zenith angle, as depicted in Figure 5.2.

5.2 Sensitivity of a Ground-Based Gamma-Ray Observatory to Neutrinos

To estimate the sensitivity of a gamma-ray ground-based observatory such as the SWGO to neutrinos we have obtained the expected neutrino event rate dN/dt expressed in equation 5.1.

[1] linear cut performed in the space $\log_{10} S_{\mu}$ vs $\log_{10} S_{em}$

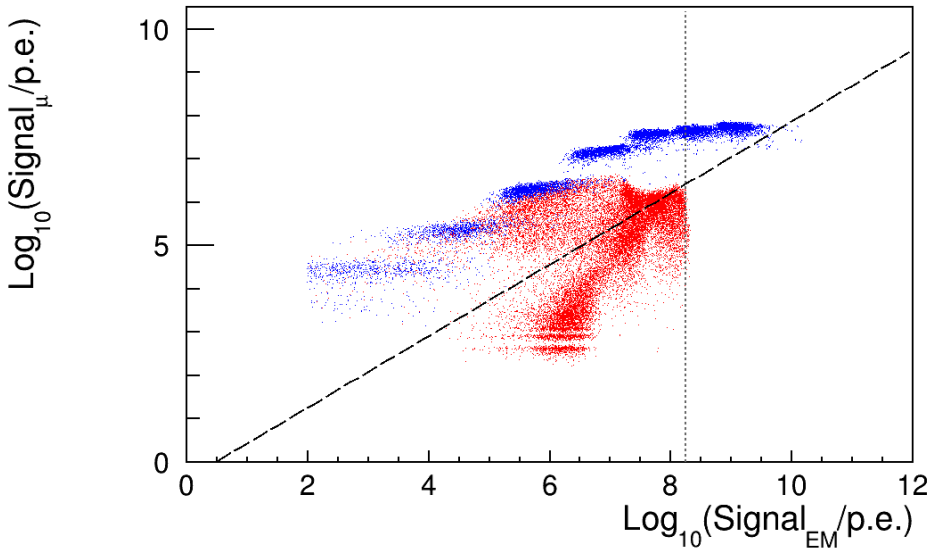

Figure 5.1: Fisher cut (dashed line) applied in the discrimination between neutrino and proton-induced showers for $\theta = 70°$. Red dots represent neutrino events while blue dots represent proton-induced showers. Dotted line corresponds to the cut in S_{em} above which neutrino-induced showers of energy below ~ 10 PeV are not expected to populate that region of the plot.

$$\frac{dN}{dt} = \int_{E_{\nu,min}}^{E_{\nu,max}} \frac{d\Phi(E_\nu)}{dE} \frac{1}{m} \sigma(E_\nu) M_{eff}(E_\nu)\, dE_\nu \tag{5.1}$$

where $d\Phi/dE$ denotes the differential flux of incoming neutrinos, m is the mass of a nucleon and $\sigma(E_\nu)$ is the neutrino cross section as a function of its energy. Moreover, $M_{eff}(E_\nu)$ is the effective mass associated with a detector as a function of the energy of the incoming neutrino, while E_{max} and E_{min} denote the integration limits used for the sensitivity calculation.

5.2.1 Dependence of Effective Mass on Shower Inclination

The effective mass is defined as the mass within which a neutrino is bound to interact and be identified. The effective mass as a function of the zenith angle (θ) and the energy of the incoming neutrino (E_ν) is expressed in equation 5.2:

$$\frac{dM_{eff}}{d\theta}(\theta, E_\nu) = \int 2\pi A \sin\theta \cos\theta\ \varepsilon(\theta, D, E_\nu)\ dD \qquad [\mathrm{g}], \tag{5.2}$$

where $\varepsilon(\theta, D, E_\nu)$ denotes the probability of detecting a neutrino with energy E_ν, injected at a zenith angle θ, and experiencing its first interaction at a slant depth of D. The detection probability is dependent on the cuts introduced to remove the hadronic background. It is a function of the slant depth of the neutrino's point of first interaction D (expressed in $\mathrm{g\,cm^{-2}}$), the energy of the neutrino E_ν (expressed in GeV) and the angle of incidence θ (expressed in radians). Being an efficiency, it assumes a value between 0 and 1. Similarly, A is the surface area of the array, initially fixed at a value of $1\mathrm{km}^2 = 10^{10}\mathrm{cm}^2$.

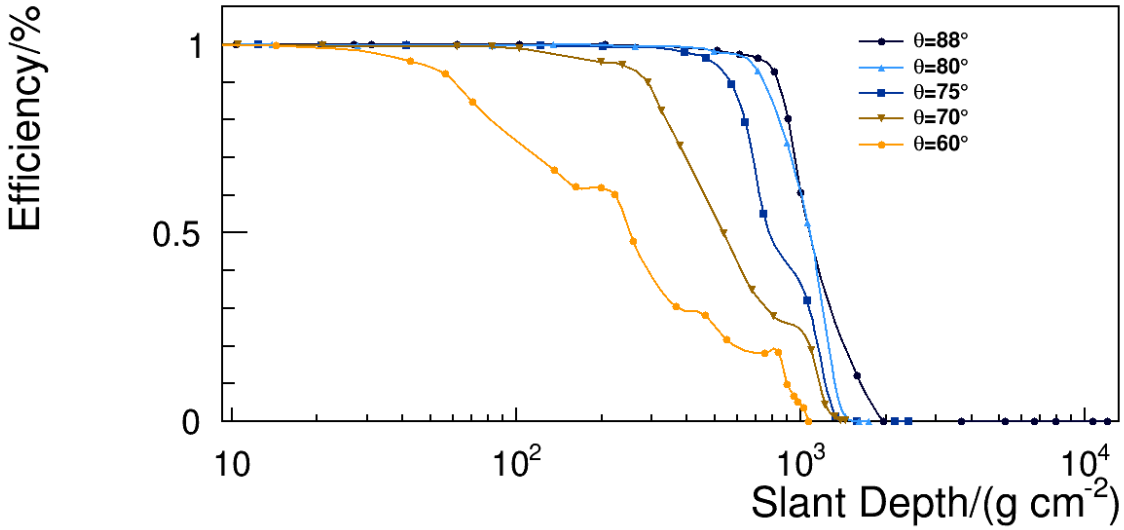

Figure 5.2: Discrimination efficiency as a function of neutrino interaction slant depth for the cases of showers induced by 1PeV neutrinos, with $\theta = 60°$, $70°$, $75°$, $80°$ and $88°$.

Starting with 1 PeV showers, five values of θ are considered: $60°$, $70°$, $75°$, $80°$ and $88°$. This wider range of values of θ, while still within the domain of inclined and very inclined showers, aims to maximise the resulting neutrino event rate. ROOT's interpolation method, *Eval*, is applied to $\varepsilon(\theta, D, E_\nu)$ (E_ν and θ are fixed within each case) in order to integrate in D. This procedure results in the effective mass values reported in Table 5.1.

Table 5.1: Effective mass for different values of θ, for neutrino-induced showers with $E_\nu = 1$PeV.

θ	$\frac{dM_{eff}}{d\theta}(\theta, E_\nu = 1\text{PeV})$ [g]
60°	9.73×10^{12}
70°	1.27×10^{13}
75°	1.65×10^{13}
80°	9.09×10^{12}
88°	2.21×10^{12}

5.2.2 Total Effective Mass

Making use of the $\frac{dM_{eff}}{d\theta}(\theta, E_\nu)$ values at 1 PeV, equation 5.2 can then be integrated in zenith angle. This calculation is done using equation 5.3, where zenith angles that were not simulated are obtained via cubic spline interpolation.

$$M_{eff}(E_\nu) = \int \frac{dM_{eff}}{d\theta}(\theta, E_\nu)\, d\theta \qquad [\text{g sr}] \tag{5.3}$$

This integration yields a total effective mass of 2.97×10^{14} g sr, a value that is assumed to remain approximately constant for small energy bins. In the present case, this applies to the $1 - 2$ PeV energy bin.

5.2.3 Neutrino Flux

The flux of neutrinos as a function of their energy is given by equation 5.4, where $E_0 = 10^6$ GeV and $k' = kE_0^{-2} = 10^{-20}\,\mathrm{GeV}^{-1}\,\mathrm{cm}^{-2}\,\mathrm{s}^{-1}\,\mathrm{sr}^{-1}$. The value of the k' constant is taken from the data made available by the IceCube Neutrino Observatory [6].

$$\frac{d\Phi}{dE}(E_\nu) = k' \left(\frac{E_\nu}{E_0}\right)^{-2} \tag{5.4}$$

5.2.4 Neutrino Cross Section

The last requirement is the cross section associated with the interaction of incoming neutrinos with the nucleons of the target medium, as a function of their energy. The values required were taken from [31]. Since the neutrino energy values considered in the present thesis are contained within the range 10 TeV to 1 EeV, the corresponding rows are taken from Table I of [31]. Within this table, the distinction between charged, neutral and total interaction is made, allowing for the plotting of the 3 curves depicted in Figure 5.3, by applying cubic spline interpolation to the existing points. The value of neutrino-nucleon interaction cross section can be determined by applying ROOT's *Eval* method to these plots.

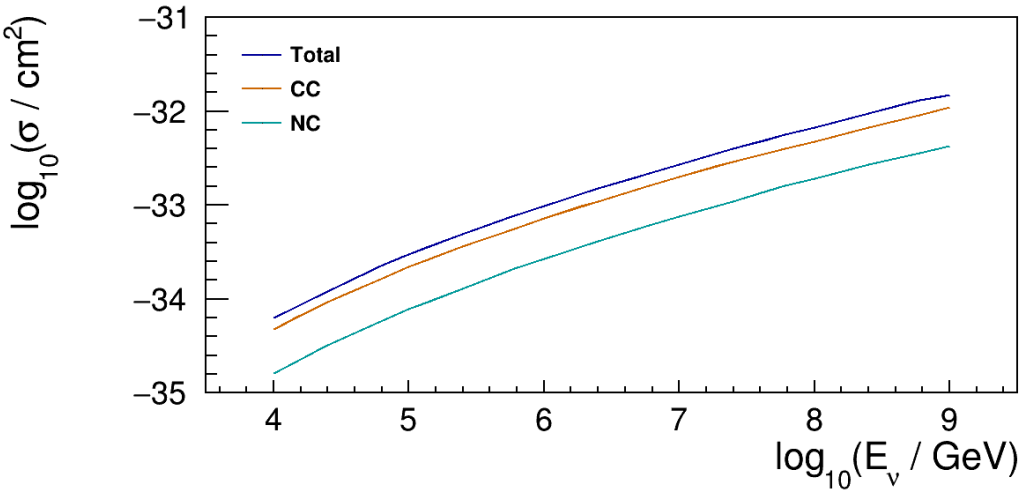

Figure 5.3: Neutrino-nucleon charged, neutral and total current cross sections. Data taken from [31]

5.2.5 Sensitivity of an EAS observatory to 1 PeV Neutrinos

As all required parameters have been estimated or described as functions of the energy of incoming neutrinos, it is possible to compute the sensitivity of a ground-based gamma-ray detector to 1 PeV neutrinos. Replacing the neutrino flux in Eq.5.2 with Eq.5.4 results in equation 5.6. The values of the parameters required for the computation of dN/dt are listed in Table 5.2.

$$\frac{dN}{dt} = \int_{E_{\nu,min}}^{E_{\nu,max}} k' \left(\frac{E_\nu}{E_0}\right)^{-2} \frac{1}{m} \sigma(E_\nu) M_{eff}(E_\nu) dE_\nu \tag{5.5}$$

$$= \frac{k' E_0^2 M_{eff}}{m} \int_{E_{\nu,min}}^{E_{\nu,max}} \frac{\sigma(E_\nu)}{E_\nu^2} dE_\nu \tag{5.6}$$

Integrating Eq.5.6 in energy between 1 and 2 PeV yields an event rate of $3.12 \times 10^{-2}\,\mathrm{yr}^{-1}$, corresponding to roughly one event every 32 years. While this value is far from optimal for an experiment, which typically has a time scale of a few decades, it should be noted that this value was obtained without accounting for the evolution of the effective mass with the energy of the neutrinos. As this quantity is expected to increase with energy, so is the number of expected neutrino events. Hence, this evolution shall be discussed in section 5.2.8.

Restricting the zenithal angle to $\theta \geq 75°$, previous calculations yield a total effective mass of $1.12 \times 10^{14}\,\mathrm{g\,sr}$, and an event rate of $1.18 \times 10^{-2}\,\mathrm{yr}^{-1}$. Both estimated event rates are of the same order of magnitude, thus showers with $\theta < 75°$ are not simulated in the study of 100 TeV neutrinos presented in section 5.2.7.

Table 5.2: Value of parameters considered in the calculation of the sensitivity of a wide-field ground-based gamma-ray observatory to 1 PeV neutrinos

Parameter	Value	Units
E_0	10^6	GeV
A	10^{10}	cm^2
m	1.67×10^{-24}	g
k'	10^{-20}	$\mathrm{GeV}^{-1}\,\mathrm{cm}^{-2}\,\mathrm{s}^{-1}\,\mathrm{sr}^{-1}$
$M_{eff}(E_0)$	2.97×10^{14}	g sr
$E_{\nu,min}$	10^6	GeV
$E_{\nu,max}$	2×10^6	GeV

5.2.6 Impact of Neutrino Interaction Channel on Sensitivity

The neutrino detection efficiency and hence the effective mass depend on the interaction channel the neutrino undergoes in order to initiate the cascade. In the cases previously described, the interaction channel, namely charged current (CC) or neutral current (NC), was randomly chosen according to their relative weight in the total cross section. However, in CORSIKA simulations the type of interactions can be set so that neutrinos only interact via CC or NC, allowing for an alternative approach to the computation of sensitivity where interaction channels are handled individually.

The neutrino detection efficiencies for the CC and NC channels applied to the case with $E_\nu = 1$ PeV are presented in Figure 5.4, where the case with random types of interaction is located between the curves associated with exclusively charged current or neutral current interactions. Integrating Eq.5.2 in zenith angle for each type of interaction yields the effective mass values reported in Table 5.3.

The sum of the effective masses obtained for the NC and CC interaction channels individually, 5.87×10^{14} g sr is larger than the effective mass associated with a random type of interaction, 2.97×10^{14} g sr.

Table 5.3: Values of effective mass for the different neutrino interaction channels CC and NC and $E_\nu = 1$PeV. Total corresponds to the case where CC or NC are chosen randomly

Interaction	$M_{eff}(E_\nu = 1\,\text{PeV})\,[\text{g sr}]$
CC	3.60×10^{14}
NC	2.27×10^{14}
Total	2.97×10^{14}

To determine whether this distinction is beneficial, the other decisive factor to consider is the interaction cross section, as given by the curves in Figure 5.3. The other remaining factor, the neutrino flux, has no dependence on the type of interaction.

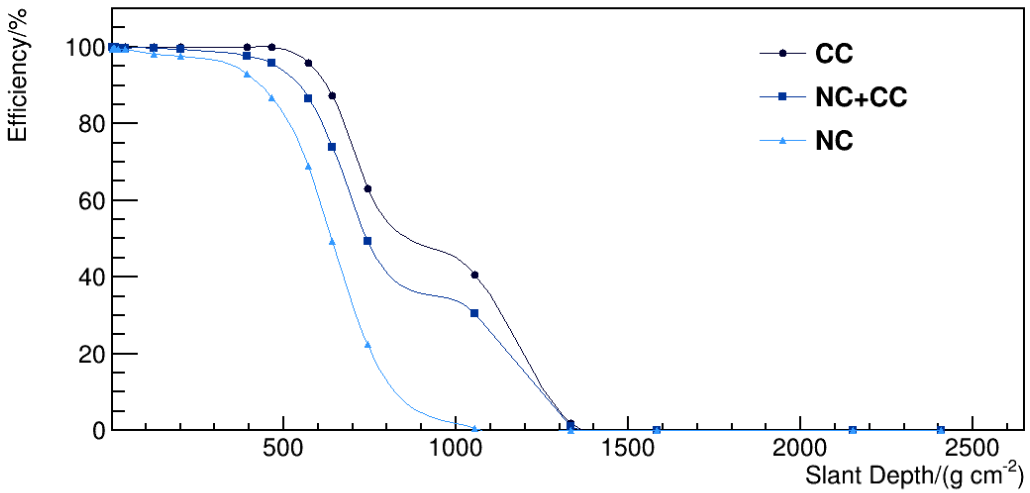

Figure 5.4: Discrimination efficiency curves obtained for showers induced by 1 PeV neutrinos with $\theta = 75°$. Interactions are either selected at random according to their cross sections (NC+CC), or set explicitly to only charged (CC) or neutral current (NC) interactions.

Employing the parameters considered for the event rate calculation in section 5.2.5 (Table 5.2) and the effective masses listed in Table 5.3, Eq.5.6 can be integrated in energy for the cases where interactions occurs via NC or CC. This procedure yields the rates listed in Table 5.4. The event rate obtained for a random interaction type, $3.12 \times 10^{-2}\,\text{yr}^{-1}$, exceeds the sum of the individual cases where the first interaction occurs exclusively via CC or NC, $2.54 \times 10^{-2}\,\text{yr}^{-1}$. This sum is roughly 18% smaller than the aforementioned value. Thus, the approach in which CC or NC are chosen according to their relative cross sections maximises the number of expected events per year.

Table 5.4: Sensitivity of a wide-field ground-based gamma-ray observatory to astrophysical neutrinos, according to the type of the first interaction. E_ν spanning from 1PeV to 2 PeV

Interaction	$\frac{dN}{dt}\,[\text{yr}^{-1}]$
CC	2.29×10^{-2}
NC	2.50×10^{-3}
Total	3.12×10^{-2}

5.2.7 Sensitivity to 100 TeV Neutrinos

A study was also carried out for neutrinos with $E_\nu = 100\,\text{TeV}$, where the atmospheric neutrino flux is expected to dominate the energy spectrum. A procedure identical to the one described in sections 5.2.1 - 5.2.5 was followed. This study only took into consideration 3 values of zenith angle $\theta = 75°$, $80°$ and $88°$, instead of the previously considered 5 values. This narrower range of θ values is more focused on the domain of very inclined showers, since the wider range of values of θ introduced in the case of 1 PeV energy did not result in a significant increase of the resulting event rate. This choice of θ also eliminates the need for cuts in the electromagnetic signal (S_{em}) for the cases with $\theta = 60°$ and $70°$, as they are not taken into account.

The resulting discrimination efficiency curves are depicted in Figure 5.5. These are then used in the procedure described in section 5.2.1 to obtain the effective mass for the 3 values of zenith angle, as listed in Table 5.5.

Table 5.5: Effective mass for different values of θ for neutrino-induced showers, with $E_\nu = 100\text{TeV}$.

θ	$\frac{dM_{eff}}{d\theta}(\theta, E_\nu = 100\text{TeV})\,[\text{g}]$
75°	1.16×10^{13}
80°	8.47×10^{12}
88°	2.18×10^{12}

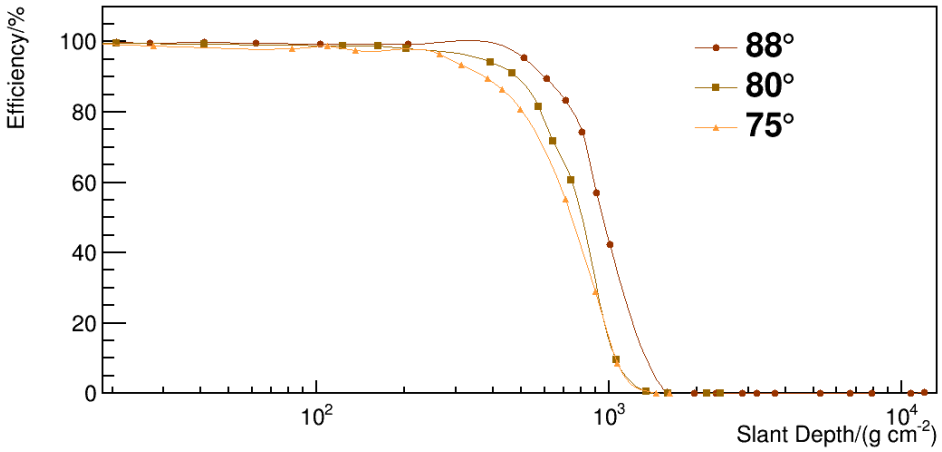

Figure 5.5: Discrimination efficiency curves obtained for the cases of showers induced by 100TeV neutrinos, with $\theta = 75°$, $80°$ and $88°$.

Taking into account the $M_{eff}(\theta, E_\nu)$ values at 100 TeV, equation 5.2 is integrated in zenith angle. Following the procedure described in section 5.2.2, this calculation is done using equation 5.3, where zenith angles between $75°$ and $88°$ that were not simulated are obtained via a cubic spline interpolation. The resulting total effective mass for $E_\nu = 100\,\text{TeV}$ is $9.55 \times 10^{13}\,\text{g sr}$, a value that is assumed to remain constant in small energy bins. In the present case, this refers to the $100 - 200\,\text{TeV}$ energy bin.

The neutrino flux as a function of neutrino energy is given by Eq.5.4 and the cross section is determined via the plots presented in Figure 5.3. The parameters necessary for the computation of the event rate and

their respective values are listed in Table 5.6. Integrating Eq.5.6 over the neutrino energy (E_ν spanning from 100TeV to 200 TeV) yields an event rate of 3.14×10^{-2} yr^{-1}, corresponding to approximately one event every 32 years, as was the case for $E_\nu = 1$ PeV. This similarity can be attributed to the evolution of the neutrino cross section, total effective mass and neutrino flux between the two energy bins. For instance, the increase in the neutrino flux between $E_\nu = 1$ PeV and 100 TeV is counterbalanced to by the decrease in the neutrino cross section and the total effective mass in the same interval.

Table 5.6: Value of parameters considered in the calculation of the sensitivity of a wide-field ground-based gamma-ray observatory to 100 TeV neutrinos.

Constant	Value	Units
E_0	10^6	GeV
A	10^{10}	cm^2
m	1.67×10^{-24}	g
k'	10^{-20}	GeV^{-1} cm^{-2} s^{-1} sr^{-1}
$M_{eff}(E_0)$	9.55×10^{13}	g sr
$E_{\nu,min}$	10^5	GeV
$E_{\nu,max}$	2×10^5	GeV

5.2.8 Evolution of the Effective Mass with the Primary Energy

It is possible to attempt to find a function to more adequately describe the growth of the effective mass with neutrino energy. To achieve this, it must first be noted that the effective mass is approximately proportional to the neutrino cross section. This parameter grows linearly with energy for energies below 100 TeV, and as the energy increases the dependence shifts towards $E_\nu^{1/3}$.

As such, a power law was fitted to the values of effective mass previously calculated for $E_\nu = 100$ TeV and for $E_\nu = 1$ PeV. This lead to the growth of effective mass with the neutrino energy being described by Eq.5.7. As there are no simulations above 1 PeV, the extrapolation towards higher energies is more uncertain. To estimate the impact of such uncertainty on the effective mass calculation, an optimistic solution ($M_{eff} \propto E_\nu$) and a pessimistic one ($M_{eff} \propto E_\nu^{1/3}$) are considered.

$$M_{eff} = \left(2.97454 \times 10^{14}\right) \times \left(\frac{E}{1\,\text{PeV}}\right)^{0.5} \tag{5.7}$$

Under these conditions, the event rate is given by Eq.5.8, as the function used to describe effective mass has an explicit dependence on energy.

$$\frac{dN}{dt} = \frac{k' E_0^2}{m} \int_{E_{\nu,min}}^{E_{\nu,max}} \frac{\sigma(E_\nu)\, M_{eff}(E_\nu)}{E_\nu^2} dE_\nu \tag{5.8}$$

Using Eq.5.8 to estimate the event rate for the cases discussed in sections 5.2.5 and 5.2.7 yields the values reported in Table 5.7 and 5.8, respectively.

For E_ν spanning from 1PeV to 2 PeV, the $M_{eff} \propto E^{0.5}$ model estimates an event every 27 years, while the case with $M_{eff} \propto E^{1/3}$ points to an event every 25 years. For E_ν spanning from 100TeV to 200 TeV, the $M_{eff} \propto E^{0.5}$ model also indicates an event every 27 years, while the $M_{eff} \propto E^{1/3}$ solution estimates

Table 5.7: Sensitivity of a wide-field ground-based gamma-ray observatory ($A = 1\,\mathrm{km}^2$) to 1 PeV neutrinos, according to the function used to describe $M_{eff}(E_\nu).E_\nu$ spanning from 1PeV to 2 PeV

Model of $M_{eff}(E_\nu)$	$\frac{dN}{dt}\,[\mathrm{yr}^{-1}]$
Constant	3.12×10^{-2}
Linear	4.09×10^{-2}
$\propto E_\nu^{0.5}$	3.70×10^{-2}
$\propto E_\nu^{1/3}$	3.58×10^{-2}

Table 5.8: Sensitivity of a wide-field ground-based gamma-ray observatory ($A = 1\,\mathrm{km}^2$) to 100 TeV neutrinos, according to the function used to describe $M_{eff}(E_\nu).E_\nu$ spanning from 100TeV to 200 TeV

Model of $M_{eff}(E_\nu)$	$\frac{dN}{dt}\,[\mathrm{yr}^{-1}]$
Constant	3.14×10^{-2}
Linear	3.45×10^{-2}
$\propto E_\nu^{0.5}$	3.67×10^{-2}
$\propto E_\nu^{1/3}$	3.82×10^{-2}

an event every 29 years. Both the $M_{eff} \propto E^{1/3}$ and $M_{eff} \propto E^{0.5}$ approaches result in an increase of the expected event rate, when compared to the case where the total effective mass remains constant.

5.2.9 Measured Integral Neutrino Flux

PeV **Neutrinos**

The estimate of sensitivity can be extended to a wider range of values of the upper energy integration limit and the area of the detector. A more realistic maximum energy value of 10 PeV is introduced, followed by an extrapolated case with an upper limit of 100 PeV and where the flux of astrophysical neutrinos is unknown. Similarly, values of the area of the detector range from $5 \times 10^4 \mathrm{m}^2$ to $10^7 \mathrm{m}^2$ ($10\,\mathrm{km}^2$). The results of these two considerations, assuming $M_{eff} \propto E^{0.5}$ as described by Eq.5.7, are presented in Figure 5.6, where the currently planned area of the SWGO ($1\mathrm{km}^2$) is also indicated.

To evaluate the impact of the choice of function used to describe the effective mass with energy, we consider the scenarios where the effective mass is constant, proportional to the energy or where it follows a power law of the kind $\propto E_\nu^{1/3}$ or $\propto E_\nu^{0.5}$. Under these conditions, the results listed in Table 5.9 are obtained:

Table 5.9: Sensitivity of a wide-field ground-based gamma-ray observatory ($A = 1\,\mathrm{km}^2$) to astrophysical neutrinos, according to the choice of function used to model $M_{eff}(E_\nu).E_\nu$ spanning from 1PeV to 10 PeV and 100 PeV

Model of $M_{eff}(E_\nu)$	$\frac{dN}{dt}(E_{\nu_{max}} = 10\,\mathrm{PeV})[\mathrm{yr}^{-1}]$	$\frac{dN}{dt}(E_{\nu_{max}} = 100\,\mathrm{PeV})[\mathrm{yr}^{-1}]$
Constant	7.12×10^{-2}	9.26×10^{-2}
Linear	1.83×10^{-1}	6.21×10^{-1}
$\propto E_\nu^{0.5}$	1.19×10^{-1}	2.20×10^{-1}
$\propto E_\nu^{1/3}$	1.06×10^{-1}	1.72×10^{-1}

Based on the results listed in Table 5.9, the most conservative sensitivity estimate is obtained when the effective mass is assumed to remain constant. The second lowest estimate results from the use of a

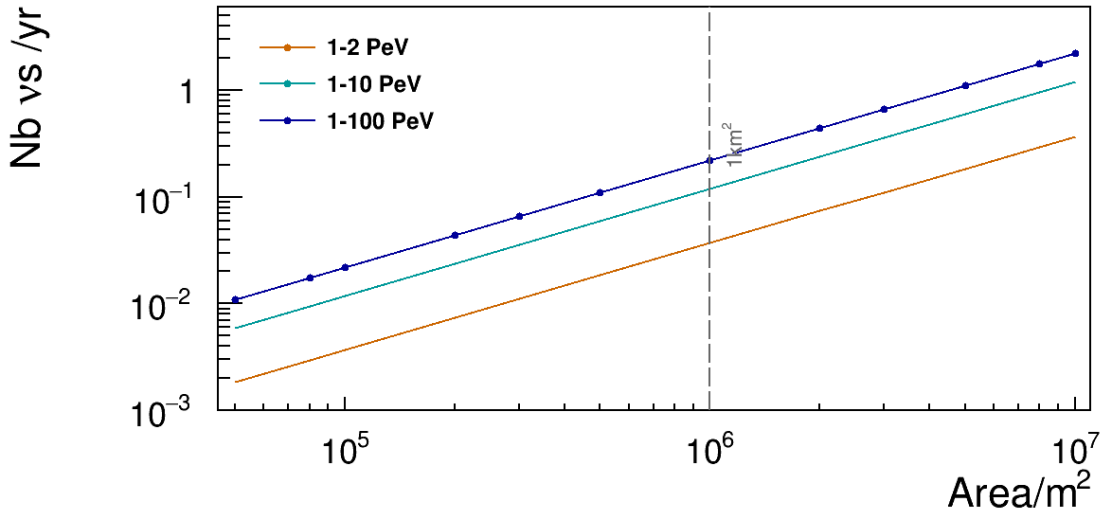

Figure 5.6: Number of astrophysical neutrinos expected to be detected and identified per year, as a function of the area of the detector. 3 curves are presented corresponding to different ranges of energies used during the sensitivity computation. At the time of writing, the SWGO is projected to have an area of 1km^2, which is indicated by a dashed vertical line. The model in which $M_{eff} \sim E_\nu^{0.5}$ is adopted.

$\propto E_\nu^{1/3}$ power law, whereas the largest value is obtained when employing a linear model. This behaviour is dominant for energies below 100 TeV, a value which is at the bottom edge of the currently considered range of energies. Given these observations and the limited amount of data available, the most reasonable approach is the one where the effective mass is assumed to follow a power law according to $E_\nu^{0.5}$. For E_ν spanning from 1PeV to 10 PeV and to 100 PeV this model estimates an event every ~ 9 and ~ 4 years, respectively.

100 TeV **Neutrinos**

The procedure followed in the previous section is now applied to the study of $E_\nu = 100$ TeV. In particular, besides the case detailed in section 5.2.7 with 100 – 200 TeV, two additional possibilities are introduced: from 100 TeV to 1 PeV, and from 100 TeV to 100 PeV. The latter case aims to encompass all possible VHE neutrino events. Plotting these three cases as functions of the detector's surface area results in the curves depicted in Figure 5.7.

The impact of the choice of the description of effective mass as a function of energy is once again be evaluated. Accounting for the same possibilities listed in the previous section, the resulting event rates are reported in Table 5.10.

The results listed in Table 5.10 follow a pattern different from that present in Table 5.9. The most conservative event rate estimate is associated with a constant effective mass for all cases. However, for $E_{\nu_{max}} = 100$ PeV, the largest value is obtained when the effective mass is assumed to grow linearly with energy, while for $E_{\nu_{max}} = 1$ PeV this occurs when it follows a $E_\nu^{1/3}$ power law. The description where

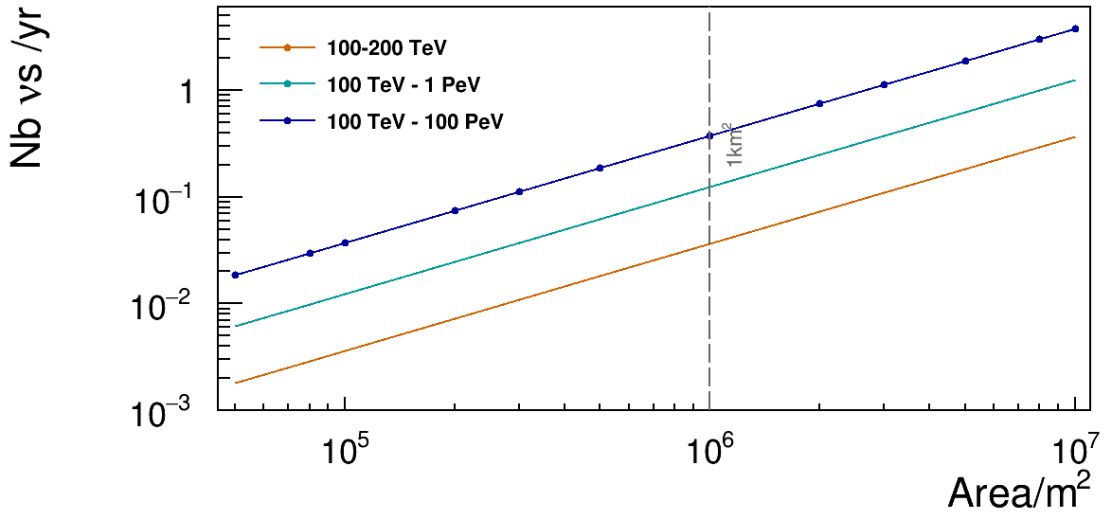

Figure 5.7: Number of atmospheric neutrinos expected to reach the detector per year, as a function of its area. 3 curves are presented corresponding to different ranges of energies used during the sensitivity calculation. At the time of writing, the detector is projected to have an area of 1km^2, which is indicated by a dashed vertical line. A model in which $M_{eff} \sim E_\nu^{0.5}$ is adopted.

Table 5.10: Sensitivity of a wide-field ground-based gamma-ray observatory ($A = 1\,\mathrm{km}^2$) to atmospheric neutrinos, according to the choice of function used to model $M_{eff}(E_\nu).E_\nu$ spanning from 100TeV to 1 PeV and 100 PeV

Model of $M_{eff}(E_\nu)$	$\frac{dN}{dt}(E_{\nu_{max}} = 1\,\mathrm{PeV})[\mathrm{yr}^{-1}]$	$\frac{dN}{dt}(E_{\nu_{max}} = 100\,\mathrm{PeV})[\mathrm{yr}^{-1}]$
Constant	8.50×10^{-2}	1.37×10^{-1}
Linear	1.13×10^{-1}	7.64×10^{-1}
$\propto E_\nu^{0.5}$	1.25×10^{-1}	3.72×10^{-1}
$\propto E_\nu^{1/3}$	1.30×10^{-1}	3.01×10^{-1}

effective mass follows a power law according to $E_\nu^{0.5}$ leads to an estimation of one event every ~ 8 and ~ 3 years for E_ν spanning from 100TeV to 1 PeV and to 100 PeV, respectively

5.3 Impact of Experimental Signal Resolution on Sensitivity

The estimations of sensitivity presented in previous sections assumed a perfect signal resolution for all components of all incoming showers. Realistically, it is necessary to account for the experimental resolution in the measurement of electromagnetic and muonic signal of incoming showers. To achieve this, study of the impact of experimental resolution in the expected event rates was carried out, by applying a Gaussian smearing to both electromagnetic and muonic signals, of both signal and background events. Denoting the fluctuations applied to the electromagnetic signal as $\sigma_{S_{em}}$ and to the muonic signal as σ_{S_μ}, the smearing is done according to a Gaussian distribution, whose mean value is the unmodified signal, as expressed by Eq. 5.9.

$$f_{S_{em}}(x) = \frac{1}{\sigma_{S_{em}}\sqrt{2\pi}} e^{-\frac{1}{2}\left(\frac{x-S_{em}}{\sigma_{S_{em}}}\right)}, \quad f_{S_\mu}(x) = \frac{1}{\sigma_{S_\mu}\sqrt{2\pi}} e^{-\frac{1}{2}\left(\frac{x-S_\mu}{\sigma_{S_\mu}}\right)} \tag{5.9}$$

Making use of this formulation, fluctuations ranging from 0 to 50% were introduced for both electromagnetic and muonic signal. Since the fluctuations are applied to both signal and background events, the offset of the associated cuts must be readjusted accordingly, in order to still ensure that background is completely eliminated. For this procedure, the vertical cuts introduced for $\theta = 60°$ and $70°$ were neglected, as such cases would require the simultaneous adjustment of two cuts. Instead, only Fisher cuts were utilised in the removal of background for all cases. While this results in slightly lower event rates, the values are still of the same order of magnitude. The impact of this readjustment in the cases of showers induced by 1PeV neutrinos injected at a $70°$ angle with $\sigma_{S_\mu} = 30\%$, $\sigma_{S_{em}} = 30\%$, and both $\sigma_{S_\mu} = 30\%$ and $\sigma_{S_{em}} = 30\%$ simultaneously, is depicted in Figures 5.8, 5.9 and 5.10 respectively. Alongside these new points, the unaltered data and its associated cut are also presented for comparison.

The result of smearing being applied to the detection of astrophysical neutrinos with energies ranging from 1 PeV to 10 PeV is presented in Figure 5.11, for the case of a detector with a surface area of 1 km^2. This plot shows that larger values of either σ_{S_μ} or $\sigma_{S_{em}}$ result in progressively lower event rates and hence lower sensitivity, as would be expected.

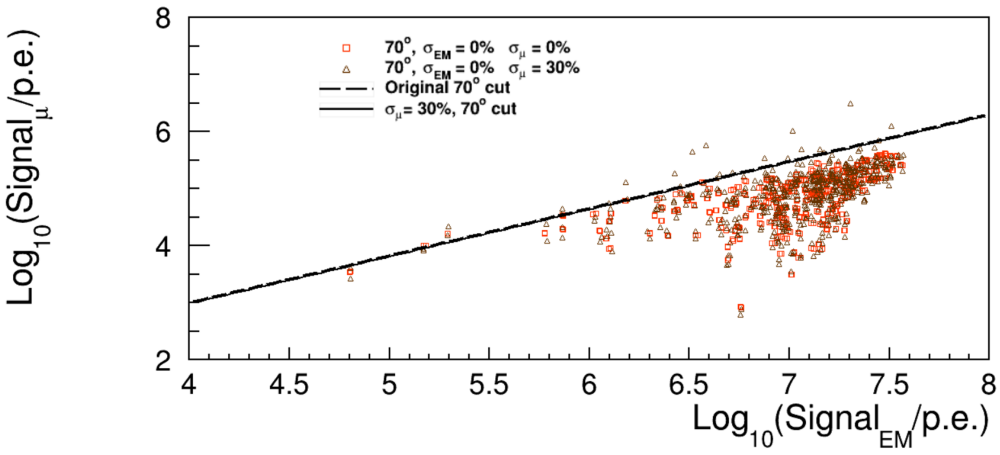

Figure 5.8: S_μ vs S_{em} for showers induced by 1PeV neutrinos injected at 70^o, with a fixed vertical interaction height of 300m above the observation level (5200m). 2 sets of points are present: in the absence of smearing, and with a Gaussian smear ($\sigma = 30\%$) applied only to the muonic signal. The 2 lines drawn represent the Fisher cut adjusted for each case to completely eliminate background.

To further explore the impact of signal fluctuations, a wider range of $\sigma_{S_{em}}$ and σ_{S_μ} was introduced, reaching a maximum value of 500%. Applying the same smearing procedure with this range of values results in the graph presented in Figure 5.12. Under these conditions, the smear applied to either the electromagnetic or muonic signal had to reach values nearing 200% in order to produce a degradation of the expected number of neutrinos by a factor of 2. This small impact of the degradation applied to the electromagnetic and muonic signal is a consequence of the cuts being applied to the logarithm of these two variables. As such, it requires fluctuations of the order of 100% to start reaching other orders of

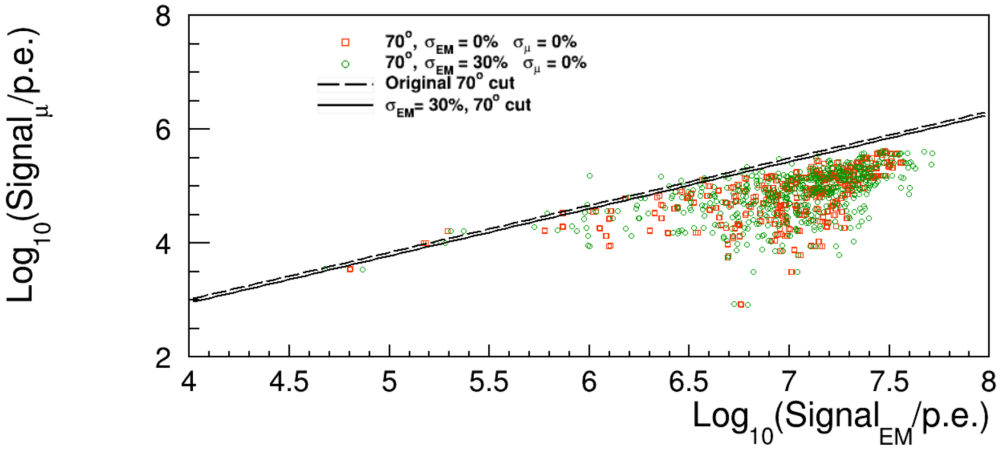

Figure 5.9: S_μ vs S_{em} for showers induced by 1PeV neutrinos injected at 70^o, with a fixed vertical interaction height of 300m above the observation level (5200m). 2 sets of points are present: in the absence of smearing, and with a Gaussian smear (σ = 30%) applied only to the electromagnetic signal. The 2 lines drawn represent the Fisher cut adjusted for each case to completely eliminate background.

magnitude, which would result in noticeable shifts of the aforementioned cuts.

5.4 Up-Going Neutrinos

One final study is carried out focusing on the viability of detecting up-going earth-skimming neutrinos, interacting underground in close proximity to the detector array (less than 5 m vertically).. Unlike the simulations used in the study of the signatures associated with down-going neutrinos, up-going neutrinos cannot be handled by CORSIKA, as it is unable to replicate atmosphere compositions that resemble that of the Earth's crust.Using the AIRES (more specifically, ZHAIRES) framework, it is possible to set the composition of the atmosphere to match that of standard soil [68], whose properties are listed in Table 5.11.

Table 5.11: Properties of the standard soil medium [68] implemented in AIRES.

Parameter	Value	Units
ρ	1.8	g cm^{-3}
Effective Z	11	–
Average Z/A	0.5	–
Rad. Length	27.6	g cm^{-2}

The framework was utilised to simulate showers generated by up-going neutrinos with an energy of 1 PeV, inclinations of $\theta = 60°, 70°, 75°, 80°$ and $88°$, and made to interact at fixed vertical heights of 2 m, 3 m and 5 m below the observation level.From the procedure described, it was possible to infer the average footprints produced in each case, and determine whether a ground-based gamma-ray observatory such as the SWGO would be capable of discerning these events. The average footprints are presented in Figures 5.13, 5.14, 5.15, 5.16 and 5.17 for the cases of up-going neutrinos with E_ν = 1 PeV, interacting at

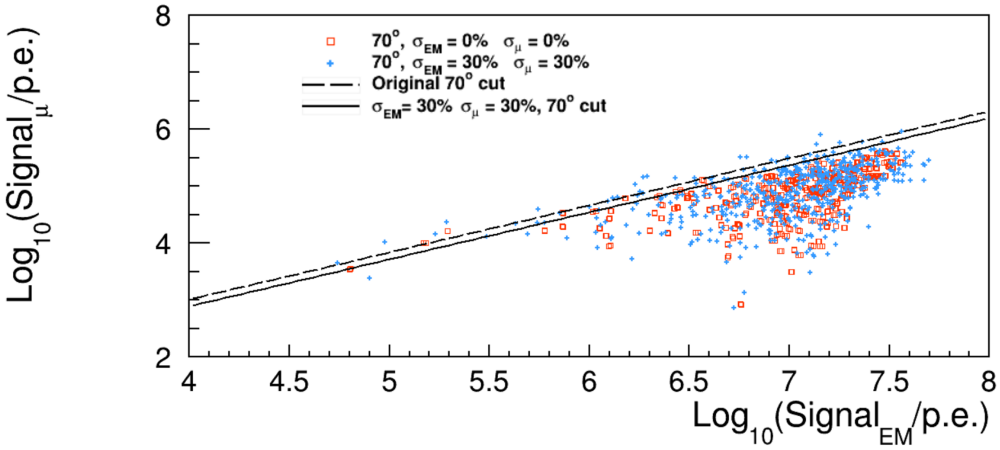

Figure 5.10: S_μ vs S_{em} for showers induced by 1PeV neutrinos injected at 70^o, with a fixed vertical interaction height of 300m above the observation level (5200m). 2 sets of points are present: in the absence of smearing, and with a Gaussian smear (σ = 30%) applied to electromagnetic and muonic signal. The 2 lines drawn represent the Fisher cut adjusted for each case to completely eliminate background.

a vertical depth of 3 m and being injected at an angle of $\theta = 60°, 70°, 75°, 80°$ and 88°, respectively.

Given the shape and small dimensions of these footprints, which are of the order of a few tens of m^2, the observatory cannot reliably detect showers generated by up-going neutrinos, since there would not be enough individual detectors triggered in a majority of cases. This is more so the case if such showers were to reach only the sparse array of the observatory, where the interval between neighbouring stations is approximately 20 m. This would result in the loss of a critical amount of data pertaining to these showers. For these reasons, considerations regarding showers induced by up-going neutrinos were discarded in the estimation of the sensitivity of an EAS array to neutrinos.

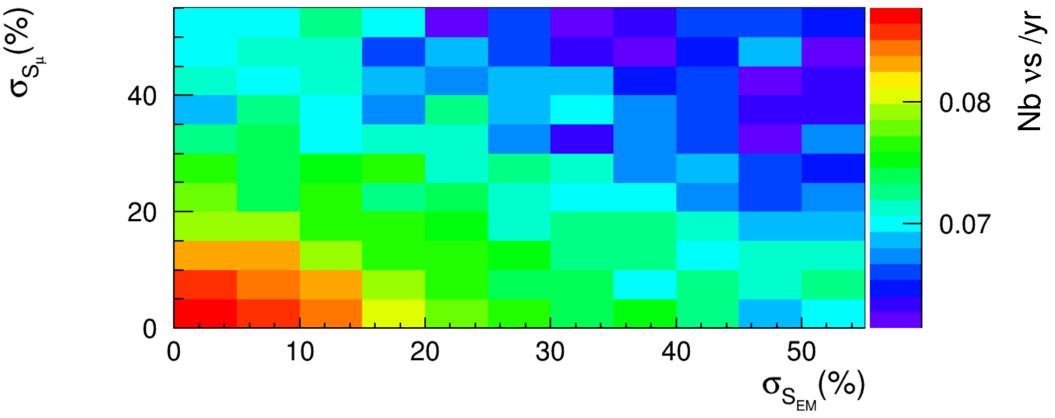

Figure 5.11: Neutrino event rate as a function of the σ of the Gaussian smearing applied to the electromagnetic and muonic signal. Calculations performed for the range of energies 1 PeV–10 PeV, assuming the detector's surface area is 1 km^2. The model of $M_{eff} \sim E_\nu^{0.5}$ has been adopted.

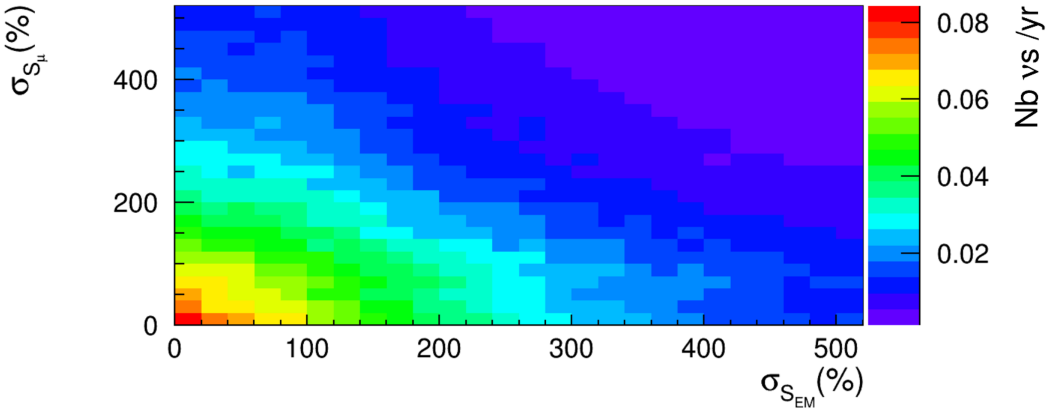

Figure 5.12: Neutrino event rate as a function of the σ of the Gaussian smearing applied to the electromagnetic and muonic signal, up to 500%. Calculations performed for the range of energies 1 PeV – 10 PeV, assuming the detector's surface area is 1 km^2. The model of $M_{eff} \sim E_\nu^{0.5}$ has been adopted.

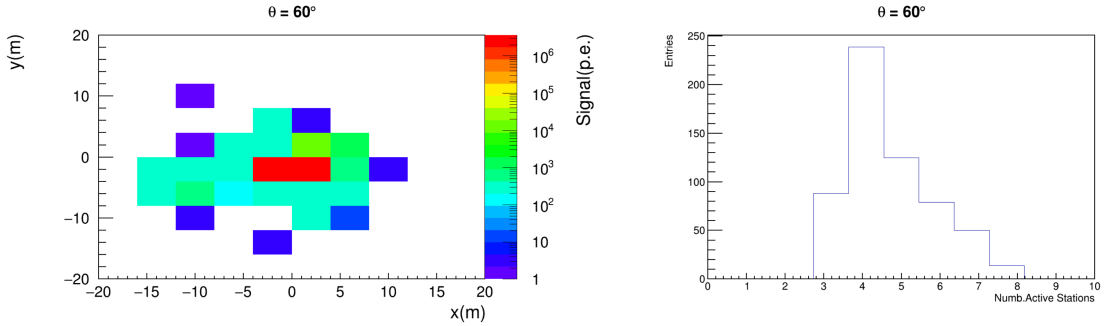

Figure 5.13: Shower induced by an up-going neutrino with E_ν = 1 PeV and $\theta = 60°$ interacting at a vertical height of 3 m below the observation level. **Left:** Average footprint. **Right:** Distribution of number of active stations per each up-going neutrino event.

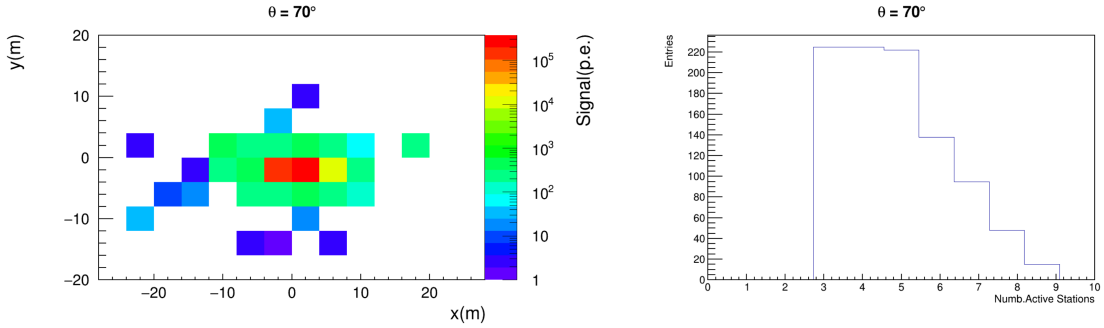

Figure 5.14: Shower induced by an up-going neutrino with $E_\nu = 1$ PeV and $\theta = 70°$ interacting at a vertical height of 3 m below the observation level. **Left:** Average footprint. **Right:** Distribution of number of active stations per each up-going neutrino event.

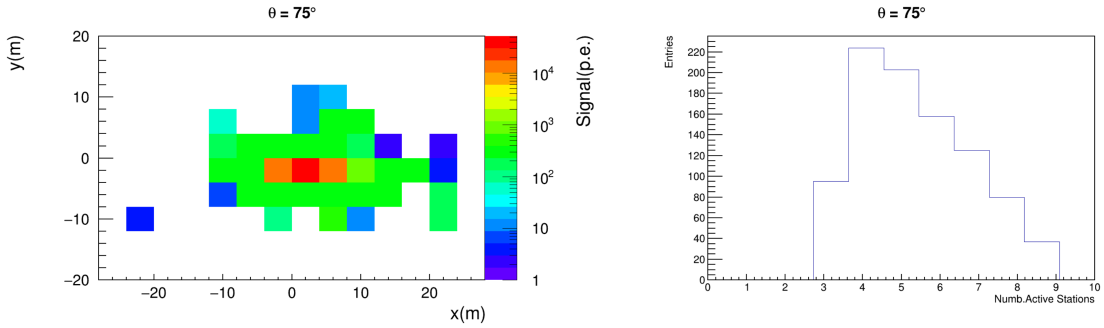

Figure 5.15: Shower induced by an up-going neutrino with $E_\nu = 1$ PeV and $\theta = 75°$ interacting at a vertical height of 3 m below the observation level. **Left:** Average footprint. **Right:** Distribution of number of active stations per each up-going neutrino event.

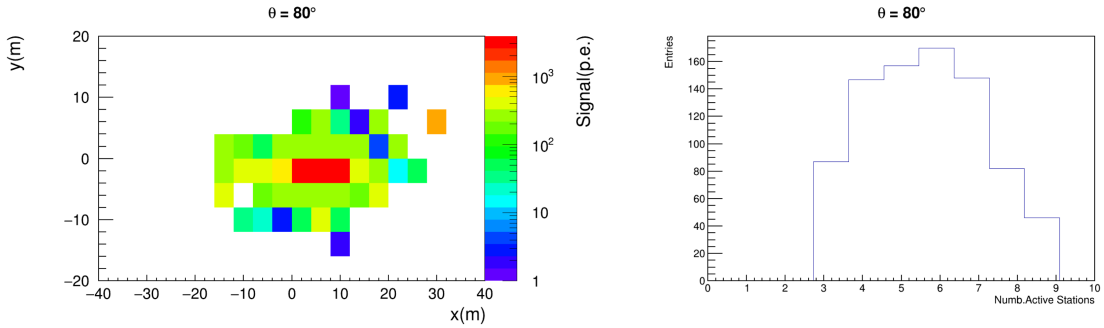

Figure 5.16: Shower induced by an up-going neutrino with $E_\nu = 1$ PeV and $\theta = 80°$ interacting at a vertical height of 3 m below the observation level. **Left:** Average footprint. **Right:** Distribution of number of active stations per each up-going neutrino event.

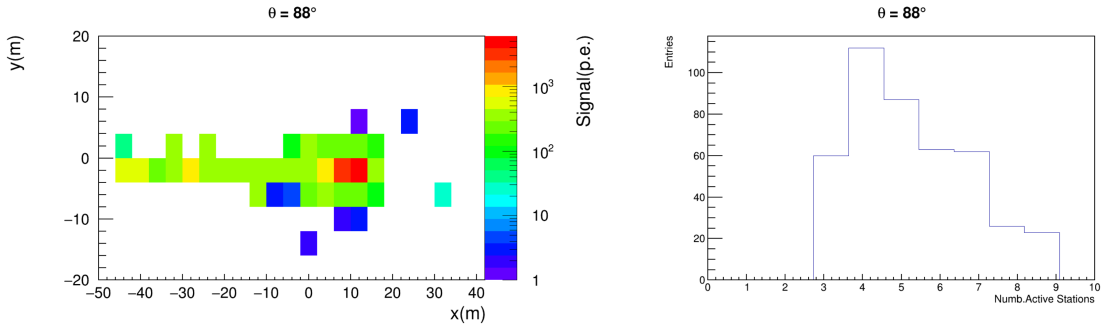

Figure 5.17: Shower induced by an up-going neutrino with $E_\nu = 1$ PeV and $\theta = 88°$ interacting at a vertical height of 3 m below the observation level. **Left:** Average footprint. **Right:** Distribution of number of active stations per each up-going neutrino event.

Chapter 6

Summary

In this thesis we have carried out a study of the sensitivity of a km^2-scale wide field ground-based gamma-ray observatory to VHE atmospheric and astrophysical neutrinos. Taking into account the results pertaining to down-going neutrinos, it is reasonable to state that such an observatory is predicted to be capable of detecting astrophysical and atmospheric neutrinos in a decade-long observation, with a high cosmic-ray background reduction.

Using a model in which $M_{eff} \propto E_\nu^{0.5}$, the event rate estimated for 1 PeV neutrinos ranges from $3.7 \times 10^{-2}\,\mathrm{yr}^{-1}$ to $2.2 \times 10^{-1}\,\mathrm{yr}^{-1}$. This correspond to one event every 27 year and every $\sim$ 5 years, respectively. The event rate expected for 100 TeV neutrinos assumes values from $3.7 \times 10^{-2}\,\mathrm{yr}^{-1}$ to $3.7 \times 10^{-1}\,\mathrm{yr}^{-1}$, when adopting a model in which $M_{eff} \propto E_\nu^{0.5}$. This translates to an event every 27 years and every $\sim$ 3 years, respectively. The latter case encompasses neutrinos with energies ranging from 100 TeV to 100 PeV, and covers all neutrino detection possibilities for the detector setup used in this work. Applying an optimistic model of the growth of the total effective mass with neutrino energy ($M_{eff} \propto E_\nu$) to this case results in an event rate of $7.6 \times 10^{-1}\,\mathrm{yr}^{-1}$. This upper bound corresponds to an event every $1 - 2$ years.

Overall, the sensitivity obtained for both 1 PeV and 100 TeV neutrinos bears a noticeable degree of similarity. These cases exhibit comparable discrimination efficiency curves (in the zenith angle range common to both studies), and the expected event rates differ by less than 1% from one another (when comparing the case of $1 - 2$ PeV and $100 - 200$ TeV with $M_{eff} \sim E_\nu^{0.5}$).

On a separate note, we studied the relative contribution of the CC and NC interaction channels to the expected astrophysical neutrino event rate. The dominating contribution in effective mass was associated with CC interactions. However, when accounting for the cross section of each interaction channel, the adoption of a more a realistic approach in which CC or NC are chosen according to their relative cross sections proved most beneficial.

We also studied the effect on the event rates of the choice of the model describing the growth of the total effective mass with the neutrino energy. When this quantity was assumed to remain constant within small energy bins, the resulting sensitivity was severely underestimated. Under these conditions, collecting $\sim$ 1 neutrino event would require a time scale comparable to or even exceeding that of a typical

experiment, thus emphasising the need to account for the evolution of the total effective mass with energy. Given the importance of this factor, two limiting cases were considered: an optimistic one where the total effective mass was assumed to evolve linearly with energy, and a pessimistic one where the total effective mass grows with $E_\nu^{1/3}$. During the present work, it became clear that additional shower simulations at around $E_\nu = 10\,\mathrm{PeV}$ would be important in avoiding extrapolation towards higher energies. The absence of these simulations results in larger uncertainty when accounting for larger energy ranges, such as $1 - 100\,\mathrm{PeV}$. This will be addressed in the future. The approach deemed most reasonable was the $M_{eff} \sim E_\nu^{0.5}$ power law fitted to the total effective mass values obtained for $E_\nu = 100\,\mathrm{TeV}$ and $1\,\mathrm{PeV}$. This function represents a halfway point between the behaviour associated with lower energies ($E_\nu < 100\,\mathrm{TeV}$, $M_{eff} \propto E_\nu$) and the one expected at higher energies ($E_\nu > 1\,\mathrm{PeV}$, $M_{eff} \propto E_\nu^{1/3}$).

Regarding the impact of the experimental resolution, it was noted that a degradation of the expected neutrino event rate by a factor of 2 would require extreme resolutions of the order of 200% for either the electromagnetic or muonic signal. Thus, experimental resolution does not appear to pose a decisive obstacle in the detection of neutrinos by ground-based gamma-ray observatories, under the conditions established in the present thesis.

Lastly, based on the results obtained from the injection of up-going neutrinos, it is clear these events do not contribute to the sensitivity of the gamma-ray observatory. This is due to the small dimensions of the footprints produced in these events, which would require a higher density of stations in the sparse array to allow for a proper detection of incoming particles. It must be noted this work did not evaluate additional possibilities that would increase the neutrino event rate, such as neutrinos interacting within geological formations, namely mountains, as this would largely depend on the topology of the site of the experiment in question. Incorporating tau neutrinos into this calculation would further increase this number. Therefore, the expected event rates reached in this thesis represent only a lower bound of the possibility of neutrino detection using an EAS array, and serve to accentuate the viability of this measurement.

Bibliography

[1] A.Aab et al. “A Search for Ultra-high-energy Neutrinos from TXS 0506+056 Using the Pierre Auger Observatory”. In: *The Astrophysical Journal* 902.2 (Oct. 2020), p. 105. ISSN: 1538-4357. DOI: 10.3847/1538-4357/abb476.

[2] A.Aab et al. “Probing the origin of ultra-high-energy cosmic rays with neutrinos in the EeV energy range using the Pierre Auger Observatory”. In: *Journal of Cosmology and Astroparticle Physics* 2019.10 (Oct. 2019), pp. 022–022. ISSN: 1475-7516. DOI: 10.1088/1475-7516/2019/10/022.

[3] A. Aab et al. “Spectral Calibration of the Fluorescence Telescopes of the Pierre Auger Observatory”. In: *Astroparticle Physics* 95 (Sept. 2017). DOI: 10.1016/j.astropartphys.2017.09.001.

[4] A. Aab et al. “Probing the origin of ultra-high-energy cosmic rays with neutrinos in the EeV energy range using the Pierre Auger Observatory”. In: *Journal of Cosmology and Astroparticle Physics* 2019.10 (Oct. 2019), p. 022. DOI: 10.1088/1475-7516/2019/10/022.

[5] M. G. Aartsen et al. “The IceCube Neutrino Observatory: Instrumentation and Online Systems”. In: *Journal of Instrumentation* arXiv:1612.05093 (Dec. 2016). DOI: 10.1088/1748-0221/12/03/P03012.

[6] R. Abbasi et al. “IceCube high-energy starting event sample: Description and flux characterization with 7.5 years of data”. In: *Phys. Rev. D* 104 (2 July 2021), p. 022002. DOI: 10.1103/PhysRevD.104.022002.

[7] P. Abreu et al. “Questions and Answers in Extreme Energy Cosmic Rays – a guide to explore the data set of the Pierre Auger Observatory”. In: *Nuclear and Particle Physics Proceedings* 273-275 (Apr. 2016), pp. 1271–1275. DOI: 10.1016/j.nuclphysbps.2015.09.203.

[8] P. Abreu et al. “Search for ultrahigh energy neutrinos in highly inclined events at the Pierre Auger Observatory”. In: *Physical Review D* 84.12, 122005 (Dec. 2011), p. 122005. DOI: 10.1103/PhysRevD.84.122005.

[9] P. Abreu et al. *The Southern Wide-Field Gamma-Ray Observatory (SWGO): A Next-Generation Ground-Based Survey Instrument for VHE Gamma-Ray Astronomy*. 2019. arXiv: 1907.07737 [astro-ph.IM].

[10] S. Agostinelli et al. “GEANT4: A Simulation toolkit”. In: *Nucl. Instrum. Meth.* A506 (2003), pp. 250–303. DOI: 10.1016/S0168-9002(03)01368-8.

[11] F. Aharonian et al. “High energy astrophysics with ground-based gamma ray detectors”. In: *Rep. Prog. Phys* 71 (Sept. 2008), pp. 96901–56. DOI: 10.1088/0034-4885/71/9/096901.

[12] V. Albanese et al. “The SNO+ experiment”. In: *Journal of Instrumentation* 16.08 (Aug. 2021), P08059. ISSN: 1748-0221. DOI: 10.1088/1748-0221/16/08/p08059.

[13] J. Allison et al. “Recent developments in Geant4”. In: *Nuclear Instruments and Methods in Physics Research Section A: Accelerators, Spectrometers, Detectors and Associated Equipment* 835 (2016), pp. 186–225. ISSN: 0168-9002. DOI: 10.1016/j.nima.2016.06.125.

[14] J. Alvarez-Muñiz et al. “Hybrid simulations of extensive air showers”. In: *Physical Review D* 66.3 (Aug. 2002). ISSN: 1089-4918. DOI: 10.1103/physrevd.66.033011.

[15] C. Aramo et al. “Earth-skimming UHE tau neutrinos at the fluorescence detector of Pierre Auger Observatory”. In: *Astroparticle Physics* 23.1 (Feb. 2005), pp. 65–77. ISSN: 0927-6505. DOI: 10.1016/j.astropartphys.2004.11.008.

[16] J.N. Bahcall and R. Davis. “Solar Neutrinos: A Scientific Puzzle”. In: *Science* 191.4224 (1976), pp. 264–267. DOI: 10.1126/science.191.4224.264.

[17] X. Bai et al. *The Large High Altitude Air Shower Observatory (LHAASO) Science White Paper*. 2019. arXiv: 1905.02773 [astro-ph.HE].

[18] I. Bartos and S. Marka. *Spectral Decline of PeV Neutrinos from Starburst Galaxies*. 2015. arXiv: 1509.00983 [astro-ph.HE].

[19] D. Bastieri et al. “The MAGIC experiment and its first results”. In: *Frontiers of Fundamental Physics* (2006), pp. 291–296. DOI: 10.1007/1-4020-4339-2_40.

[20] A. Bellerive et al. “The Sudbury Neutrino Observatory”. In: *Nuclear Physics B* 908 (July 2016), pp. 30–51. ISSN: 0550-3213. DOI: 10.1016/j.nuclphysb.2016.04.035.

[21] I.A. Belolaptikov et al. “The Baikal underwater neutrino telescope: Design, performance, and first results”. In: *Astroparticle Physics* 7.3 (Aug. 1997), pp. 263–282. DOI: 10.1016/S0927-6505(97)00022-4.

[22] M. Benzke et al. “Prompt neutrinos from atmospheric charm in the general-mass variable-flavor-number scheme”. In: *Journal of High Energy Physics* 2017.12 (Dec. 2017). ISSN: 1029-8479. DOI: 10.1007/jhep12(2017)021.

[23] A. Bulmahn and M.H. Reno. “Secondary atmospheric tau neutrino production”. In: *Phys. Rev. D* 82 (5 Sept. 2010), p. 057302. DOI: 10.1103/PhysRevD.82.057302.

[24] Z. Cao et al. “Ultrahigh-energy photons up to 1.4 petaelectronvolts from 12 γ-ray Galactic sources”. In: *Nature* 594 (June 2021), pp. 33–36. DOI: 10.1038/s41586-021-03498-z.

[25] A. N. Cillis et al. “Influence of the LPM effect and dielectric suppression on particle air showers”. In: *Phys. Rev. D* 59 (11 May 1999), p. 113012. DOI: 10.1103/PhysRevD.59.113012.

[26] Gen2 Collaboration and M.G. Aartsen et al. *IceCube-Gen2: A Vision for the Future of Neutrino Astronomy in Antarctica*. 2014. arXiv: 1412.5106 [astro-ph.HE].

[27] IceCube Collaboration. “Evidence for High-Energy Extraterrestrial Neutrinos at the IceCube Detector”. In: *Science* 342.6161 (2013). DOI: 10.1126/science.1242856.

[28] IceCube Collaboration. “Multimessenger observations of a flaring blazar coincident with high-energy neutrino IceCube-170922A”. In: *Science* 361.6398 (2018). ISSN: 0036-8075. DOI: 10.1126/science.aat1378.

[29] Pierre Auger Collaboration. In: *Nuclear Instruments and Methods in Physics Research Section A: Accelerators, Spectrometers, Detectors and Associated Equipment* 798 (Oct. 2015), pp. 172–213. ISSN: 0168-9002. DOI: 10.1016/j.nima.2015.06.058.

[30] R. Conceição et al. “Muon identification in a compact single-layered water Cherenkov detector and gamma/hadron discrimination using machine learning techniques”. In: *Eur. Phys. J. C* 81.6 (2021), p. 542. DOI: 10.1140/epjc/s10052-021-09312-4. arXiv: 2101.10109 [physics.ins-det].

[31] A. Connolly, R.S. Thorne, and D. Waters. “Calculation of high energy neutrino-nucleon cross sections and uncertainties using the Martin-Stirling-Thorne-Watt parton distribution functions and implications for future experiments”. In: *Physical Review D* 83.11 (June 2011), p. 113009. DOI: 10.1103/PhysRevD.83.113009.

[32] K. Eguchi et al. “First Results from KamLAND: Evidence for Reactor Antineutrino Disappearance”. In: *Phys. Rev. Lett.* 90 (2 Jan. 2003), p. 021802. DOI: 10.1103/PhysRevLett.90.021802.

[33] R. A. Fisher. “The Use of Multiple Measurements in Taxonomic Problems”. In: *Annals of Eugenics* 7.2 (1936), pp. 179–188. DOI: https://doi.org/10.1111/j.1469-1809.1936.tb02137.x.

[34] S. Fukuda et al. “The Super-Kamiokande detector”. In: *Nuclear Instruments and Methods in Physics Research Section A: Accelerators, Spectrometers, Detectors and Associated Equipment* 501.2 (2003), pp. 418–462. ISSN: 0168-9002. DOI: 10.1016/S0168-9002(03)00425-X.

[35] T.K. Gaisser and M. Honda. “Flux of atmospheric neutrinos”. In: *Annual Review of Nuclear and Particle Science* 52.1 (Dec. 2002), pp. 153–199. ISSN: 1545-4134. DOI: 10.1146/annurev.nucl.52.050102.090645.

[36] V.N. Gavin. “Contribution of gallium experiments to the understanding of solar physics and neutrino physics”. In: *Phys. Atom. Nuclei* 76 (10 Mar. 2013), pp. 1238–1243. DOI: 10.1134/S106377881309007X.

[37] D. Gottschall et al. *The Mirror Alignment and Control System for CT5 of the H.E.S.S. experiment*. 2015. arXiv: 1509.04100 [astro-ph.IM].

[38] K. Greisen. “End to the Cosmic-Ray Spectrum?” In: *Phys. Rev. Lett.* 16 (17 Apr. 1966), pp. 748–750. DOI: 10.1103/PhysRevLett.16.748.

[39] F. Halzen and D. Hooper. “High-energy neutrino astronomy: the cosmic ray connection”. In: *Reports on Progress in Physics* 65.7 (June 2002), pp. 1025–1078. ISSN: 0034-4885. DOI: 10.1088/0034-4885/65/7/201.

[40] S. Harm et al. “Characteristics of extensive air showers around the energy threshold for ground-particle-based γ-ray observatories”. In: *Eur. Phys. J. C* 79 (2019), p. 427. DOI: 10.1140/epjc/s10052-019-6942-x.

[41] D. Heck et al. *CORSIKA: A Monte Carlo Code to Simulate Extensive Air Showers,” Report FZKA 6019, Forschungszentrum Karlsruhe*. 1998.

[42] W. Heitler. *The Quantum Theory of Radiation*. Oxford University Press, 1954.

[43] J.J. Hernández Rey et al. "Search for neutrino non-standard interactions with ANTARES and KM3NeT-ORCA". In: *Journal of Instrumentation* 16.09 (Sept. 2021), p. C09016. ISSN: 1748-0221. DOI: 10.1088/1748-0221/16/09/c09016.

[44] A. Hoecker et al. "TMVA - Toolkit for Multivariate Data Analysis". In: 2007.

[45] *IceCube - South Pole Neutrino Observatory*. URL: https://icecube.wisc.edu/science/icecube/ (visited on 10/22/2021).

[46] F. Kaether et al. "Reanalysis of the Gallex solar neutrino flux and source experiments". In: *Physics Letters B* 685.1 (Feb. 2010), pp. 47–54. ISSN: 0370-2693. DOI: 10.1016/j.physletb.2010.01.030.

[47] U.F. Katz and Ch. Spiering. "High-energy neutrino astrophysics: Status and perspectives". In: *Progress in Particle and Nuclear Physics* 67.3 (July 2012), pp. 651–704. ISSN: 0146-6410. DOI: 10.1016/j.ppnp.2011.12.001.

[48] L. Lu and T. Yuan. "The use of Cherenkov light in the detection of high-energy cosmic rays and neutrinos: The Pierre Auger and IceCube Observatories". In: *Nuclear Instruments and Methods in Physics Research Section A: Accelerators, Spectrometers, Detectors and Associated Equipment* 970 (2020). A RICH LEGACY, p. 163678. ISSN: 0168-9002. DOI: https://doi.org/10.1016/j.nima.2020.163678.

[49] M.Ajello et al. "Fermi-LAT observations of High-Energy γ-ray emission toward the galactic centre". In: *The Astrophysical Journal* 819.1 (Feb. 2016), p. 44. ISSN: 1538-4357. DOI: 10.3847/0004-637x/819/1/44.

[50] M.Ajello et al. "The Fourth Catalog of Active Galactic Nuclei Detected by the Fermi Large Area Telescope". In: *The Astrophysical Journal* 892.2 (Apr. 2020), p. 105. ISSN: 1538-4357. DOI: 10.3847/1538-4357/ab791e.

[51] M.G.Aartsen et al. "Characteristics of the Diffuse Astrophysical Electron and Tau Neutrino Flux with Six Years of IceCube High Energy Cascade Data". In: *Physical Review Letters* 125.12 (2020). DOI: 10.1103/physrevlett.125.121104.

[52] M.G.Aartsen et al. "The contribution of Fermi-2LAC blazars to diffuse TeV-PeV neutrino flux". eng. In: *The Astrophysical Journal* 835.1 (2017), p. 17. ISSN: 0004-637X.

[53] J. Matthews. "A Heitler model of extensive air showers". In: *Astroparticle Physics* 22.5 (2005), pp. 387–397. ISSN: 0927-6505. DOI: https://doi.org/10.1016/j.astropartphys.2004.09.003. URL: https://www.sciencedirect.com/science/article/pii/S0927650504001598.

[54] A. B. Migdal. "Bremsstrahlung and Pair Production in Condensed Media at High Energies". In: *Phys. Rev.* 103 (6 Sept. 1956), pp. 1811–1820. DOI: 10.1103/PhysRev.103.1811.

[55] P.Billoir and O.B.Bigas. "The Pierre Auger Observatory and Neutrinos". In: *Nuclear Physics B - Proceedings Supplements* 168 (2007). Proceedings of the Neutrino Oscillation Workshop, pp. 225–231. ISSN: 0920-5632. DOI: https://doi.org/10.1016/j.nuclphysbps.2007.02.082.

[56] N. Park. *Performance of the VERITAS experiment*. 2015. arXiv: 1508.07070 [astro-ph.IM].

[57] L. Pasquali, M. H. Reno, and I. Sarcevic. “Atmospheric neutrinos from charm”. In: *Second international workshop on particle physics and the early universe (COSMO-98)* (1999). DOI: 10.1063/1.59421.

[58] S. Pastor. “Neutrino searches at the Pierre Auger Observatory”. In: *Nuclear Physics B - Proceedings Supplements* 235-236 (2013). The XXV International Conference on Neutrino Physics and Astrophysics, pp. 358–363. ISSN: 0920-5632. DOI: https://doi.org/10.1016/j.nuclphysbps.2013.04.033.

[59] Hyper-Kamiokande Proto-Collaboration and K. Abe et al. *Hyper-Kamiokande Design Report*. 2018. arXiv: 1805.04163 [physics.ins-det].

[60] R. R. Atkins et al. “TeV gamma-ray survey of the northern hemisphere sky using the Milagro observatory”. In: *Astrophysical Journal* 608.2 I (June 2004), pp. 680–685. ISSN: 0004-637X. DOI: 10.1086/420880.

[61] F. Reines and C.L. Cowan. “Detection of the Free Neutrino”. In: *Phys. Rev.* 92 (3 Nov. 1953), pp. 830–831. DOI: 10.1103/PhysRev.92.830.

[62] G.D. Sciascio. *Highlights from the ARGO-YBJ experiment*. 2010. arXiv: 1012.4400 [astro-ph.HE].

[63] “Science with the Cherenkov Telescope Array”. In: (Feb. 2018). DOI: 10.1142/10986.

[64] S. J. Sciutto. “AIRES: A system for air shower simulations”. In: (Nov. 1999). DOI: 10.13140/RG.2.2.12566.40002. arXiv: astro-ph/9911331.

[65] F.W. Stecker. “Note on high-energy neutrinos from active galactic nuclei cores”. In: *Physical Review D* 72.10 (Nov. 2005). ISSN: 1550-2368. DOI: 10.1103/physrevd.72.107301.

[66] M. Stein et al. *Ultrahigh energy cosmic rays and high energy astrophysical neutrinos*. 2021. arXiv: 2108.05512 [astro-ph.HE].

[67] A.P. Szabo and R.J. Protheroe. “Implications of particle acceleration in active galactic nuclei for cosmic rays and high energy neutrino astronomy”. In: *Astroparticle Physics* 2.4 (Oct. 1994), pp. 375–392. ISSN: 0927-6505. DOI: 10.1016/0927-6505(94)90027-2.

[68] M. Tueros and S. Sciutto. “TIERRAS: A package to simulate high energy cosmic ray showers underground, underwater and under-ice”. In: *Computer Physics Communications* 181.2 (2010), pp. 380–392. DOI: https://doi.org/10.1016/j.cpc.2009.09.022.

[69] H.L. Vargas. *Prospects of Earth-skimming neutrino detection with HAWC*. 2019. arXiv: 1908.07622 [physics.ins-det].

[70] X. Wang and Z. Dai. “Prompt TeV neutrinos from the dissipative photospheres of gamma-ray bursts”. In: *The Astrophysical Journal* 691.2 (Jan. 2009), pp. L67–L71. ISSN: 1538-4357. DOI: 10.1088/0004-637x/691/2/l67.

[71] B. Wolfe et al. “Neutrinos and Gamma Rays from Galaxy Clusters”. In: *The Astrophysical Journal* 687.1 (Nov. 2008), pp. 193–201. ISSN: 1538-4357. DOI: 10.1086/591723.

[72] Enrique Zas. “Neutrino detection with inclined air showers”. In: 7 (May 2005), pp. 130–130. DOI: 10.1088/1367-2630/7/1/130.

[73] G.T. Zatsepin and V.A. Kuz’min. “Upper limit of the spectrum of cosmic rays”. In: *JETP Lett.* 4.78 (Aug. 1966).

[74] Y. Zhang et al. “Performance of new 8-inch photomultiplier tube used for the Tibet muon-detector array”. In: *Journal of Instrumentation* 11.06 (June 2016), P06016–P06016. ISSN: 1748-0221. DOI: 10.1088/1748-0221/11/06/p06016.

[75] P.A. Zyla et al. “Review of Particle Physics”. In: *PTEP* 2020.8 (2020), p. 083C01. DOI: 10.1093/ptep/ptaa104.

Appendix A

Cuts applied to each S_{EM} vs S_{μ} graph

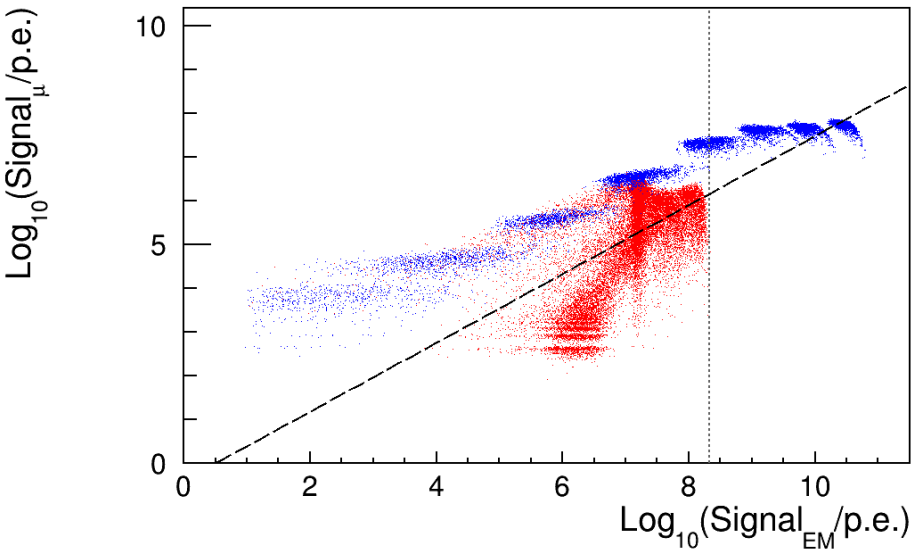

Figure A.1: Fisher cut (dashed line) applied in the discrimination between neutrino and proton-induced showers for $\theta = 60°$, $E_{\nu} = 1$ PeV. Red dots represent neutrino events while blue dots represent proton-induced showers. Dotted line corresponds to the cut in S_{em} above which neutrino-induced showers of energy below ~ 10 PeV are not expected to populate that region of the plot.

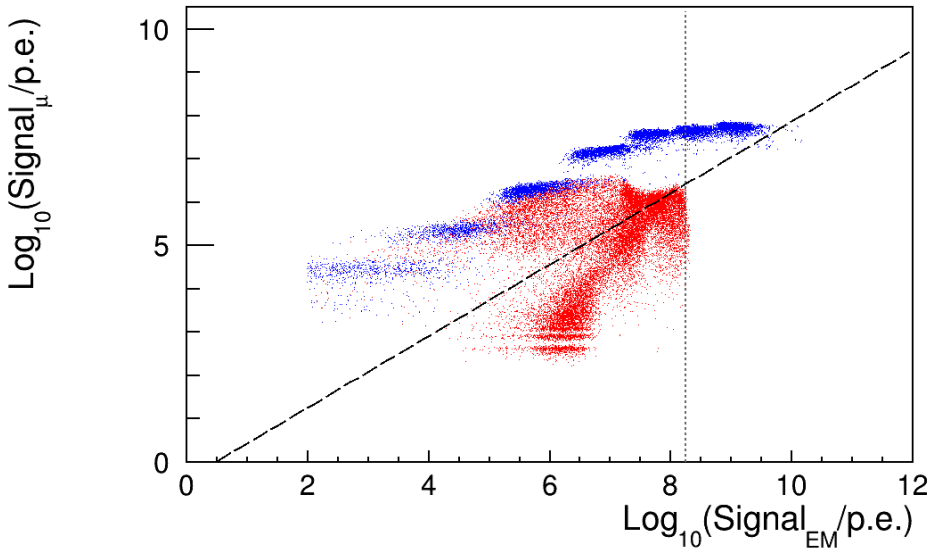

Figure A.2: Fisher cut (dashed line) applied in the discrimination between neutrino and proton-induced showers for $\theta = 70°$, $E_\nu = 1$ PeV. Red dots represent neutrino events while blue dots represent proton-induced showers. Dotted line corresponds to the cut in S_{em} above which neutrino-induced showers of energy below ~ 10 PeV are not expected to populate that region of the plot.

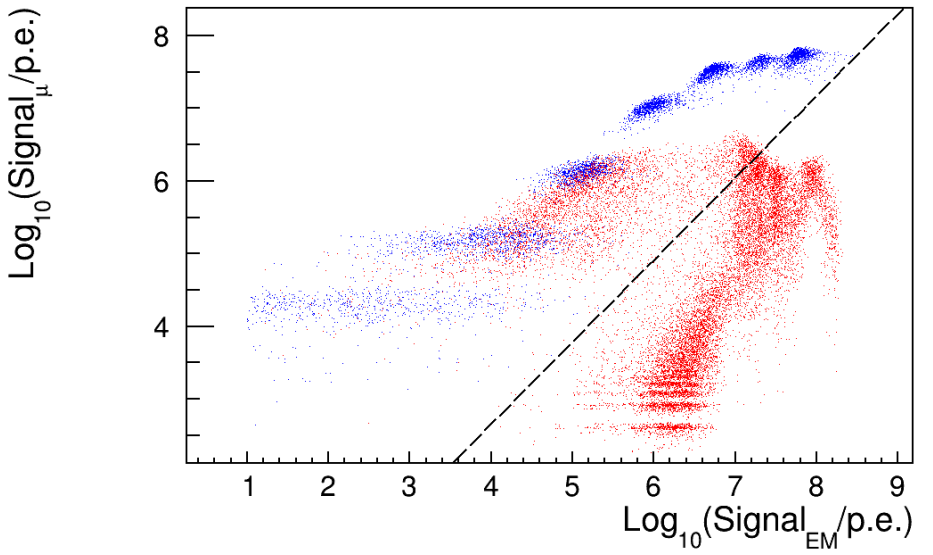

Figure A.3: Fisher cut (dashed line) applied in the discrimination between neutrino and proton-induced showers for $\theta = 75°$, $E_\nu = 1$ PeV. Red dots represent neutrino events while blue dots represent proton-induced showers.

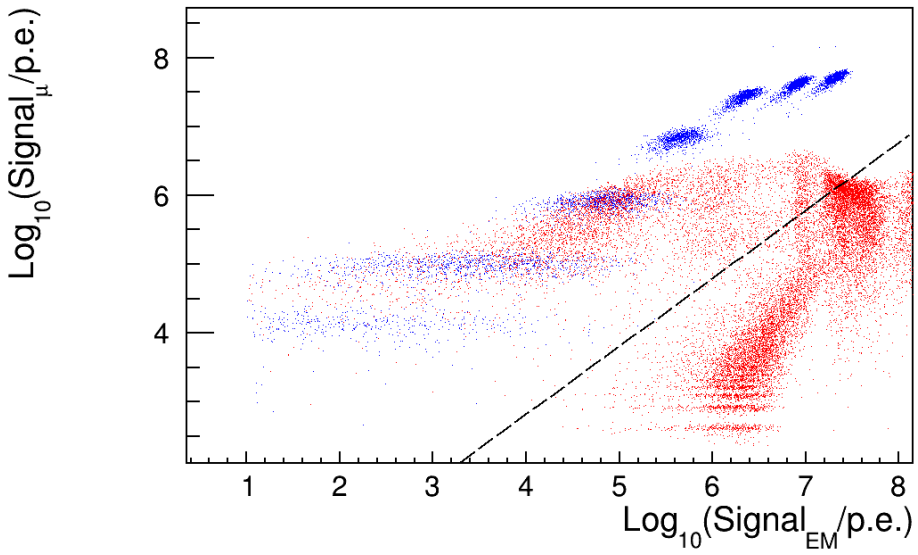

Figure A.4: Fisher cut (dashed line) applied in the discrimination between neutrino and proton-induced showers for $\theta = 80°$, $E_\nu = 1\,\text{PeV}$. Red dots represent neutrino events while blue dots represent proton-induced showers.

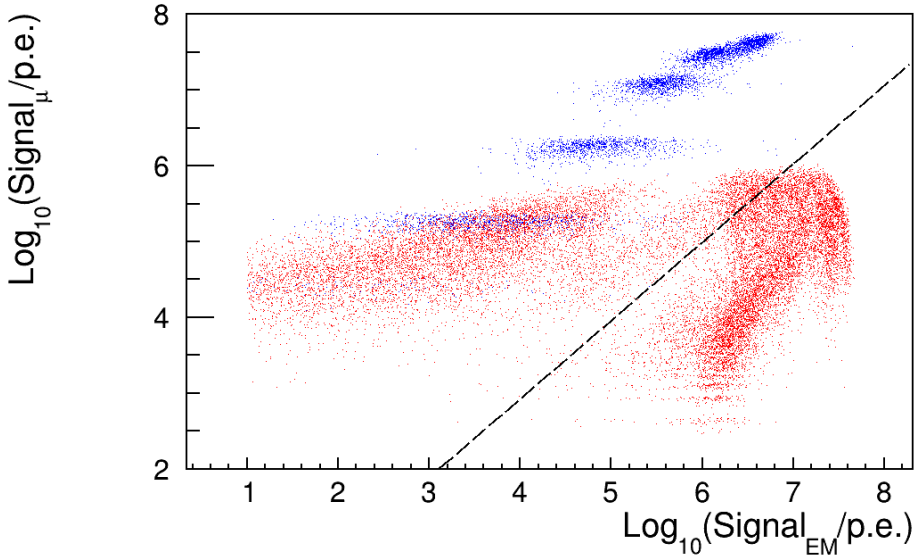

Figure A.5: Fisher cut (dashed line) applied in the discrimination between neutrino and proton-induced showers for $\theta = 88°$, $E_\nu = 1\,\text{PeV}$. Red dots represent neutrino events while blue dots represent proton-induced showers.

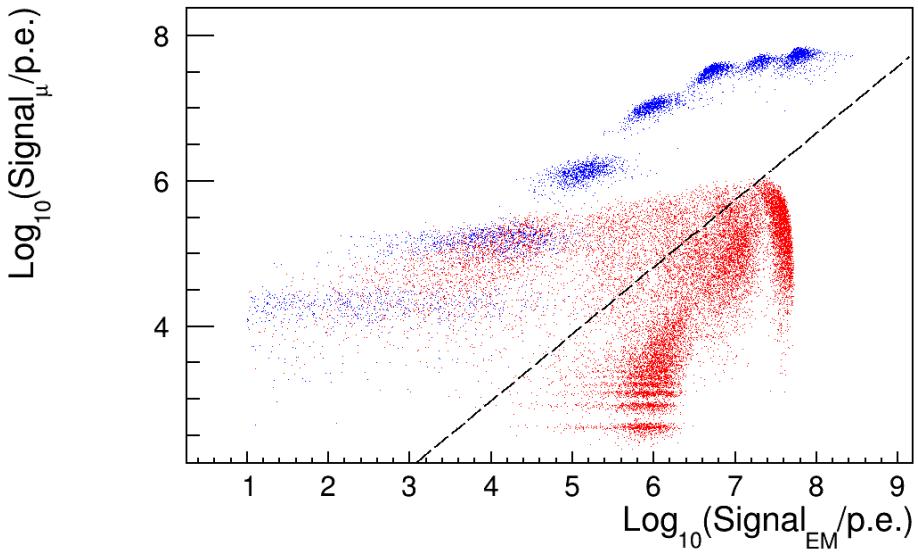

Figure A.6: Fisher cut (dashed line) applied in the discrimination between neutrino and proton-induced showers for $\theta = 75°$, $E_\nu = 100\,\text{TeV}$. Red dots represent neutrino events while blue dots represent proton-induced showers.

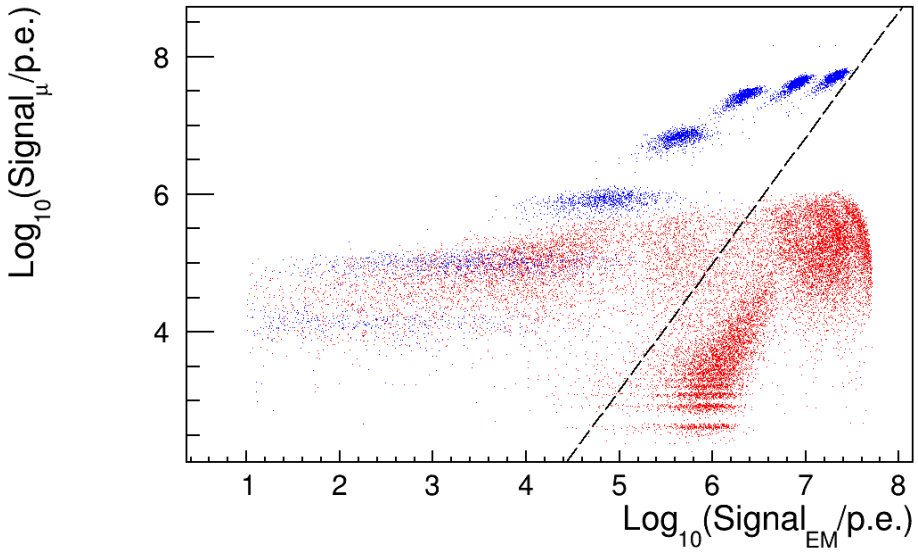

Figure A.7: Fisher cut (dashed line) applied in the discrimination between neutrino and proton-induced showers for $\theta = 80°$, $E_\nu = 100\,\text{TeV}$. Red dots represent neutrino events while blue dots represent proton-induced showers.

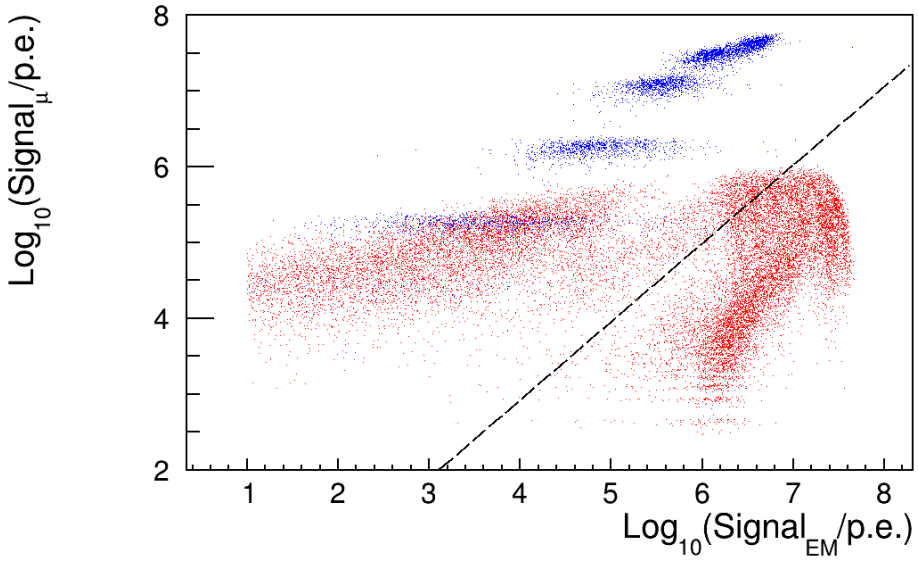

Figure A.8: Fisher cut (dashed line) applied in the discrimination between neutrino and proton-induced showers for $\theta = 88°$, $E_\nu = 100\,\text{TeV}$. Red dots represent neutrino events while blue dots represent proton-induced showers.